UNIVERSIDADE DE LISBOA
FACULDADE DE CIÊNCIAS
DEPARTAMENTO DE ENGENHARIA GEOGRÁFICA, GEOFÍSICA E ENERGIA

Improving Land Surface Temperature Retrievals Under High Concentrations of Dust Aerosols

Francesco Stante

Mestrado em Ciências Geofísicas
Especialização em Meteorologia e Oceanografia

Dissertação orientada por:
Doutora Sofia Nunes Lorena Ermida
Professor Doutor Carlos Do Carmo De Portugal E Castro Da Camara

2023

Dedicação e Agradecimentos

À Doutora Sofia Ermida, pela colaboração.
Ao Professor Carlos da Camara, pela inspiração.
À Doutora Isabel Trigo, pela orientação.
A todos os educadores que tive, pelo conhecimento.

À minha mãe e ao meu pai, pela minha vida.
Ao meu irmão e à minha irmã, pela minha personalidade.
Aos meus amigos e familiares, pelas memórias.

Dedication and Acknowledgments

To Dr. Sofia Ermida, for the collaboration.
To Prof. Carlos da Camara, for the inspiration.
To Dr. Isabel Trigo, for the guidance.
To all the educators I had, for the knowledge.

To my mother and father, for my life.
To my brother and sister, for shaping my personality.
To my friends and family, for the memories.

This work was performed within the framework of the LSA SAF project, funded by EUMETSAT, at the Portuguese Institute for Sea and Atmosphere (IPMA), through the grant IPMA-2021-017-BI.

Abstract

Current operational land surface temperature (LST) products based on thermal infrared (TIR) observations do not account for the effect of high aerosol concentrations in the atmosphere during retrievals, which reduces their utility for applications with high accuracy requirements. In this work, an analysis of the radiative effect of Saharan dust aerosols on satellite-based measurements of surface-emitted TIR radiation is presented, followed by an attempt to improve LST retrievals under heavy dust aerosol loadings by exploring an aerosol-dependent generalized split-window (GSW) algorithm.

The analysis of the radiative effect of aerosols is performed using radiative transfer simulations with the fast radiative transfer model RTTOV. These simulations show that dust aerosols, similarly to water vapor, cause differential absorption of the surface-emitted TIR radiation in the two bands usually employed for the split-window approach, around 10.8 μm and 12.0 μm. The differential absorption by dust aerosols, however, is opposite to that by water vapor, leading to an incorrect atmospheric correction performed by the GSW algorithm when dust aerosol concentrations are high, which in turn cause an underestimation of LST.

Based on this finding and given the characteristic ability of the split-window approach to address atmospheric attenuation by exploiting differential absorption, a novel calibration of the GSW algorithm is explored by adding a dependency of the algorithm coefficients on dust aerosol optical depth (DuAOD). The DuAOD-dependent GSW algorithm shows promising results, indicating improvements in LST accuracy by 2 °C or more for DuAOD values above 0.4. Since the total land area where DuAOD reaches values of 0.4 or above is extensive, encompassing all global hot deserts and the surrounding regions affected by long-range advection of dust, the implementation of a (dust) aerosol-robust retrieval algorithm in operational LST products can significantly enhance their overall accuracy and increase their utility for applications such as global climate studies.

Keywords: Land surface temperature, Aerosols, Remote sensing, Generalized Split-Window Algorithm

Resumo

A temperatura da superfície do solo (ou LST, do inglês *land surface temperature*) é uma variável importante da superfície terrestre que governa as trocas de água e energia entre a superfície e a atmosfera através da evapotranspiração, fluxos radiativos e fluxos de calor turbulentos. A única forma prática de se obter uma cobertura global e continua de LST é através de estimativas a partir de satélite. Estas são habitualmente baseadas em medições radiométricas na janela atmosférica do infravermelho térmico (ou TIR, do inglês *thermal infrared*) que abrange os comprimentos de onda 8 a 13 μm. A extensa cobertura espacial e temporal proporcionada por medições de satélite permite a utilização de LST no estudo do clima da Terra, na análise de climas urbanos ou ainda na monitorização de campos agrícolas ou incêndios florestais.

Apesar dos atuais produtos operacionais de LST, baseados em medições de satélite, terem incertezas abaixo de 1 °C em condições de céu limpo, os métodos de estimativa de LST ainda têm algumas limitações que reduzem a sua precisão em certas condições. Uma limitação é a estimativa de LST durante elevadas concentrações de poeiras. Atualmente, os algoritmos de estimativa de LST utilizados em contextos operacionais não consideram inteiramente o efeito de aerossóis e vários estudos indicam que estes produtos têm erros significativos em situações de elevada concentração de aerossóis. No sentido de melhorar as estimativas de LST nessas condições, esta dissertação apresenta um estudo do efeito radiativo de um tipo de aerossóis— as poeiras — sobre estimativas de LST e explora uma forma de melhorar essas estimativas através de uma calibração do algoritmo *generalized split-window* (GSW) dependente da concentração de aerossóis.

A análise do efeito radiativo das poeiras é realizada através de simulações com o modelo de transferência radiativa RTTOV. As simulações mostram que este tipo de aerossóis, tal como o vapor de água, causam absorção diferencial da radiação TIR emitida pela superfície nas duas bandas geralmente utilizadas na técnica *split-window*, em torno de 10.8 e 12.0 μm. Contudo, como a absorção diferencial das poeiras é oposta à do vapor de água, a correção atmosférica realizada pelo algoritmo GSW, quando as concentrações de aerossóis são elevadas, é incorreta e resulta na subestimação da LST. Esta absorção diferencial correspondente a uma diminuição da transmissividade da atmosfera mais intensa no canal dos 10.8 do que dos 12.0 μm. Quando a concentração de poeiras, exprimido pela espessura ótica (ou DuAOD, do inglês *dust aerosol optical depth*), é elevada (DuAOD ≈ 2.0), a transmissividade do canal 10.8 μm pode diminuir até 40%. Isto significa que, nestas condições, de toda a radiação TIR emitida pela superfície somente 60% chega ao topo da atmosfera (ou TOA, do inglês *top of the atmosphere*) e é medida pelo sensor abordo do satélite. No entanto, as simulações mostram que para DuAOD ≈ 2.0 a diminuição de radiância total que atinge o TOA é de cerca 4%, devendo-se ao aumento de emissão por parte dos aerossóis suspensos na atmosfera que balançam a redução de radiação vinda da superfície.

Com base na absorção diferencial das poeiras revelada pelas simulações com o RTTOV, tendo em conta que a abordagem *split-window* tem a capacidade característica de corrigir a atenuação atmosférica com base na absorção diferencial, é explorada uma nova calibração do algoritmo GSW, adicionando uma dependência dos coeficientes GSW em DuAOD. Para esse efeito criou-se uma base de dados de calibração que representa uma ampla gama de condições atmosféricas e de superfície para várias classes de DuAOD, de forma a de garantir a robustez do algoritmo em todos os cenários possíveis. A seleção dessas condições é realizada utilizando uma metodologia que calcula a dissimilaridade entre duas condições atmosféricas com base nos perfis de temperatura, humidade e aerossóis. Como os perfis de temperatura têm uma variabilidade vertical muito diferente da humidade e dos aerossóis, o peso que os

perfis de cada variável têm sobre o cálculo da dissimilaridade entre duas condições atmosféricas não é igual. Na sua forma original desta metodologia, que não inclui os perfis de aerossóis, os perfis de temperatura têm um peso igual a um e os perfis de humidade têm um peso igual a 1/9. Para esta nova base de dados, onde os perfis de aerossóis têm de ser incluídos, foram testados três pesos diferentes (0.1, 0.2 e 0.3) para os aerossóis, mantendo os pesos dos perfis de temperatura e humidade da metodologia original. Um peso maior implica que as diferenças entre os perfis de aerossóis têm mais importância no calcula da dissimilaridade entre duas condições atmosféricas do que um peso menor. Uma análise das condições selecionadas com os três pesos mostra que um peso maior melhora a representatividade dos perfis de aerossóis, mas diminui a representatividade dos perfis de temperatura. Por outro lado, um peso menor melhora a representatividade dos perfis de temperatura, diminuindo a representatividade dos perfis de aerossóis. Os perfis de humidade não são significativamente afetados pelos diferentes pesos. Com base nesta análise, escolheu-se o valor intermédio (0.2) para criar a base de dados de calibração. Os dados atmosféricos e de superfície são obtidos, respetivamente, da 4ª-geração da reanálise global de composição atmosférica da CAMS (*Copernicus Atmosphere Monitoring Service*), EAC4, e da 5ª-geração da reanálise climática do Centro Europeu de Previsão do Tempo a Médio Prazo (ou ECMWF, do inglês *European Centre for Medium-Range Weather Forecasts*), ERA5.

Com esta nova base de dados calibrou-se um algoritmo GSW com dependência no DuAOD, lembrando que um GSW tradicional só tem dependência no conteúdo atmosférico de vapor de água, no ângulo de visão do satélite e na emissividade. O desempenho deste novo algoritmo é testado face a um algoritmo GSW tradicional que não inclui aerossóis no processo de calibração. O algoritmo GSW dependente de DuAOD apresenta resultados promissores, indicando melhorias na precisão da LST de pelo menos 2 °C para valores de DuAOD acima de 0.4. Uma vez que a área total da terra onde DuAOD atinge valores de 0.4 ou mais é extensa, abrangendo todos os desertos quentes globais e as regiões circundantes afetadas pela advecção das poeiras, a implementação de um algoritmo para a estimativa de LST que seja robusto às poeiras (e outros tipos de aerossóis) pode melhorar significativamente a precisão geral dos produtos de LST e aumentar sua utilidade para aplicações como estudos climáticos.

Apesar destes resultados promissores, trabalhos futuros terão de considerar diversos aspetos antes da implementação desta metodologia para a estimativa de LST em condições em que a concentração de aerossóis é elevada. Por exemplo, a precisão das estimativas de LST num contexto operacional utilizando um algoritmo GSW dependente de DuAOD dependerá da precisão das previsões de DuAOD utilizadas. Assim sendo, é necessário realizar uma análise de sensibilidade de forma a determinar o impacto das incertezas do DuAOD nas precisões da LST. Este tipo de análise também permitirá definir o limiar de DuAOD acima do qual o novo algoritmo GSW tem um desempenho melhor do que um GSW tradicional, tendo em conta as incertezas dos algoritmos e das previsões de DuAOD. Além disso, uma vez que a correção atmosférica realizada pelo GSW assume uma linearidade na absorção diferencial pelo vapor de água, é necessário investigar se essa linearidade também ocorre no caso das poeiras. Se esse não for o caso, uma formulação diferente do *split-window* poderá ter um desempenho melhor do que o GSW dependente do DuAOD apresentado neste trabalho.

Palavras-Chave: Temperatura da superfície do solo, Aerossóis, Deteção remota, Algoritmo Generalized Split-Window

Table of Contents

List of Figures

List of Acronyms and Abbreviations

BT	Brightness Temperature
CAMS	Copernicus Atmosphere Monitoring Service
DuAOD	Dust Aerosol Optical Depth
EAC4	CAMS' Fourth-Generation Global Reanalysis on Atmospheric Composition
ECMWF	European Centre for Medium-Range Weather Forecasts
ERA5	ECMWF's Fifth-Generation Climate Reanalysis
EUMETSAT	European Organization for the Exploitation of Meteorological Satellites
GSW	Generalized Split-Window
JPL	NASA's Jet Propulsion Laboratory
LSA SAF	Satellite Applications Facility on Land Surface Analysis
LST	Land Surface Temperature
MSG	Meteosat Second Generation
NASA	National Aeronautics and Space Administration
NWP SAF	Satellite Application Facility on Numerical Weather Prediction
RTM	Radiative Transfer Model
RTTOV	Fast RTM developed by NWP SAF
SEVIRI	Spinning Enhanced Visible and Infrared Imager
SZA	Satellite Zenith Angle
TCWV	Total Column Water Vapor
TIR	Thermal Infrared
TOA	Top of the Atmosphere
Tskin	Skin Temperature

Chapter 1 — Introduction

1.1 Land Surface Temperature

Land surface temperature (LST) is an important variable of Earth's land surface. It determines the radiation emitted by the surface through Planck's Law and drives latent heat (through evapotranspiration) and sensible heat exchanges between the surface and the atmosphere [1]–[6]. Space-borne instruments are uniquely capable of providing continuous and global measurements of LST, which are essential for the study of Earth's climate and can also serve to study urban climates [7]–[9], agricultural and ecological systems [10]–[14], or even monitor burned areas [15], [16].

Satellite-based LSTs are commonly estimated from radiometric measurements in the thermal infrared (TIR) atmospheric window (8–13 μm), where Earth's surface emission is highest and atmospheric absorption is lowest. In order to generate accurate LST products on an operational basis, the surface, atmospheric, and directional effects must be accounted for using efficient retrieval algorithms [17].

1.2 Impact of Aerosols on Satellite-based LST Retrievals

Although current LST products have uncertainties around 1 °C for retrievals under clear-sky conditions [18]–[22], they still have some limitations which reduce their accuracy in specific conditions. One limitation of LST products is retrievals under heavy aerosol loadings, since the effect of aerosols is not fully considered in current operational LST retrieval algorithms [17], [23]. All TIR-based LST products that do not address this issue likely have significant errors in areas with high concentrations of aerosols [24].

In contrast, *sea* surface temperature (SST) products have considered the impact of aerosols on satellite-based TIR measurements for a long time. Research on the impact of aerosols on SST dates back to the 1980s [25]–[27], when eruptions from major volcanos produced stratospheric volcanic aerosols which were found to cause systematic underestimations of SST by as much as 7 °C. Since the accuracy requirements of SST for global climate studies is specified to be around 0.1 °C and retrievals failed to meet these requirements in the presence of the volcanic aerosols, multiple aerosol-robust SST retrieval algorithms and aerosol-correction schemes were developed and have since been used [25]–[34].

Concerning LST retrievals, only moderate attention has been given to this issue over the past decade [35]–[41], almost exclusively to the effect of dust aerosols, which are one of the most abundant types of aerosols by mass and have the highest maximum optical thickness of all aerosol types [42]. The existing studies have primarily performed radiative transfer simulations of the impact of aerosols on LST retrievals, indicating that — similarly to SST retrievals — LST is increasingly underestimated as aerosol loadings increase. Some of these studies have also investigated methods to correct the effect of dust aerosols. Fan et al. (2015) [36] found errors of up to 5.12 K when the aerosol optical depth (AOD) in the atmosphere is 1.0 and satellite zenith angle (SZA) is 60°, and proposed a correction scheme based on a linear relationship between the LST error and AOD, achieving improvements around 4 K for AOD = 1.0 and SZA = 60°. Fan et al. (2018) [38] investigated a three-channel algorithm using the TIR channels centered at 11 and 12.0 μm (commonly used for LST retrievals) and a channel centered at 8.55 μm, which is less affected by dust aerosols. One advantage of this algorithm is not requiring AOD as

input, in contrast to the linear relationship by Fan et al. (2015). In terms of performance, it is more accurate for wet atmospheres than the correction scheme by Fan et al (2015) but less accurate for dry atmospheres. Zhao et al. (2020) [39] explored a four-channel algorithm combining two middle infrared (MIR: 3-5 μm) and two TIR channels and achieved RMSE around 2 K for an AOD of 1.0 at nadir. Although the proposed solutions have limitations, they show that substantial improvements to LST accuracies are attainable.

To assess the impact of dust aerosols on LST retrievals that do not considering their effect, Stante et al. (2023) [24] examined commonly-used products over the Sahara Desert and Sahel region — where high concentrations of dust aerosols are prevalent [43], [44] (Fig. 1.1). The LST products are compared against the skin temperature (Tskin) from ECMWF's fifth-generation climate reanalysis (ERA5), which is a useful reference to diagnose the potential impact of dust aerosols over an area with scarce in situ measurements. Three LST products are analyzed: (i) the product developed by the European Organization for the Exploitation of Meteorological Satellites (EUMETSAT) Satellite Applications Facility on Land Surface Analysis (LSA SAF) [45], based on observations from the Spinning Enhanced Visible and InfraRed Imager (SEVIRI) on board Meteosat Second Generation (MSG) satellites, which uses a Generalized Split-Window (GSW) algorithm [46], [47] for LST estimation; (ii) & (iii) two products from NASA's Jet Propulsion Laboratory (JPL), based on observations from the Moderate Resolution Imaging Spectroradiometer (MODIS) onboard the Terra and Aqua satellites, the first using a GSW algorithm [48], [49] and the second employing the Temperature-Emissivity Separation (TES) technique [50], [51].

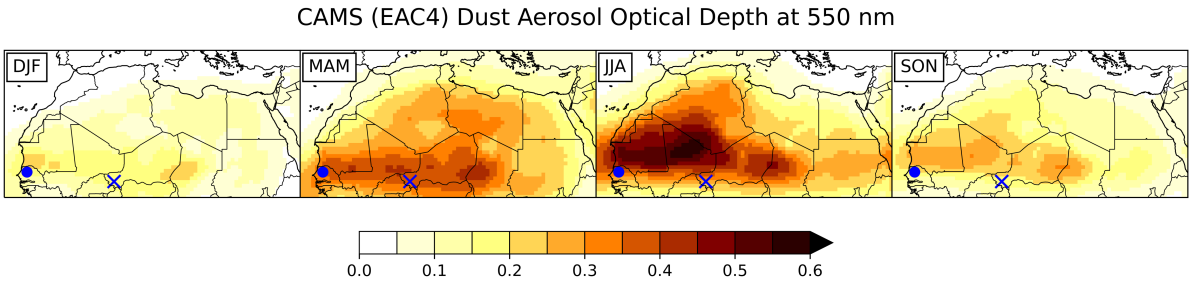

Figure 1.1 — Seasonal averages of dust aerosol optical depth (DuAOD) at 550 nm from the fourth-generation global reanalysis on atmospheric composition (EAC4) from the Copernicus Atmosphere Monitoring Service (CAMS) over the Sahara Desert and Sahel region for years 2006-2013. Values are unitless. The two ground stations available for in situ LST during this period are marked on the map: Niamey, Niger (cross); Dahra, Senegal (dot). Adapted from [24].

The LST products and ERA5's Tskin are compared by calculating their differences (LST Delta) over the Sahara and Sahel for the years 2006 and 2009 to 2013 (to be compatible with available in situ measurements). Seasonal averages of LST Delta for each LST product, shown in Fig. 1.2, have a striking similarity with seasonal maps of dust aerosol optical depth (DuAOD), shown in Fig. 1.1. The strong negative values of LST Delta during the months June-to-August coincide with the period of largest dust activity and indicate a substantial underestimation of LST of over 5 °C, if the modelled Tskin is assumed to not be impacted by the aerosols. Because water vapor and dust aerosols have a similar seasonality in this region, and since water vapor is the main atmospheric constituent affecting TIR-based LST estimations, the relation between LST Delta values and atmospheric water vapor content is also examined but is shown to have a weak relation to the underestimated LSTs.

To confirm these findings, recognizing that ERA5's Tskin cannot be considered an absolute reference to satellite-based LST estimations — as it is based on a complex surface model with limitations in its

representation of surface conditions and interactions with the atmosphere — in situ estimates of LST are used as an independent reference to both satellite LSTs and ERA5's Tskin. The biases (LST Error) between all the products and in situ LST from the station in Dahra, Senegal, are shown in Fig. 1.3 as a function of DuAOD and confirm that satellite-based LSTs are underestimated when concentrations of dust aerosols are high. In contrast, ERA5's Tskin errors show no relation with DuAOD. The maps in Fig. 1.2 are, therefore, a good indication of the spatial (and temporal) extent of aerosol-induced LST underestimation across North Africa. Note that for product MxD11, the year-long biases in the transition zone between the Sahara Desert and the Sahel region are due to mis-representation of emissivities in the LST product and not related to dust aerosols.

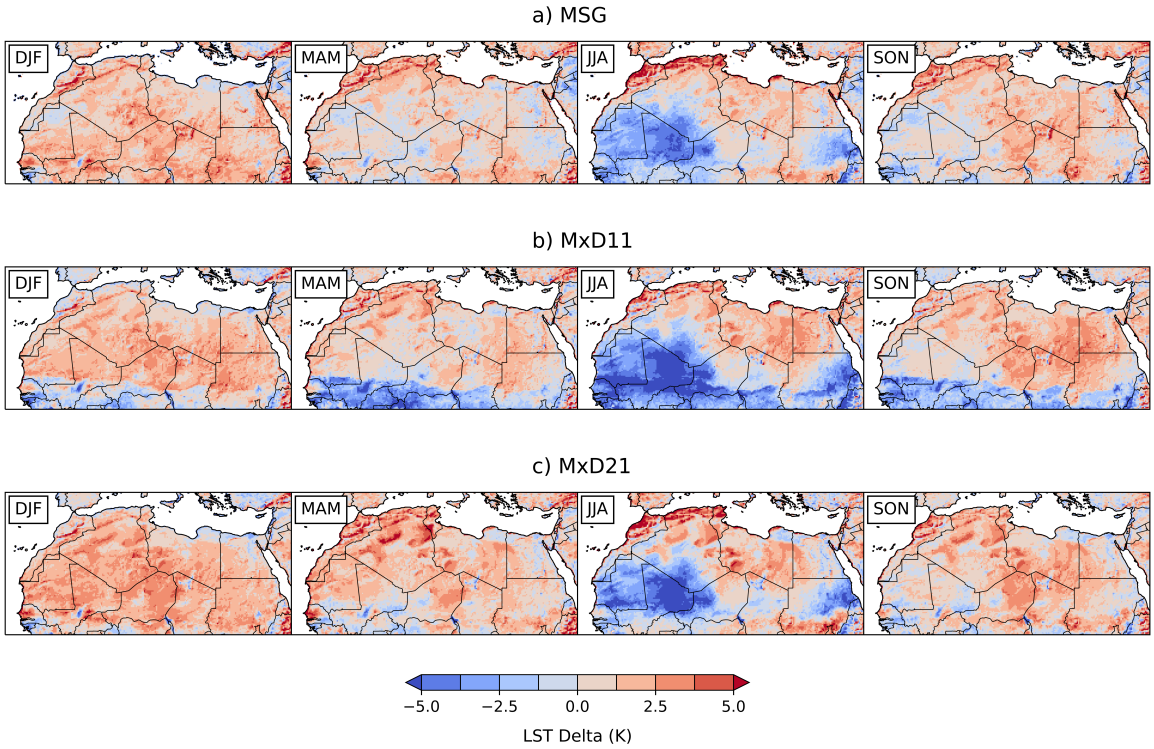

Figure 1.2 — Seasonal averages of LST Delta for years 2006 and 2009 to 2013 for three LST products: (a) MSG; (b) MxD11; and (c) MxD21. Adapted from [24].

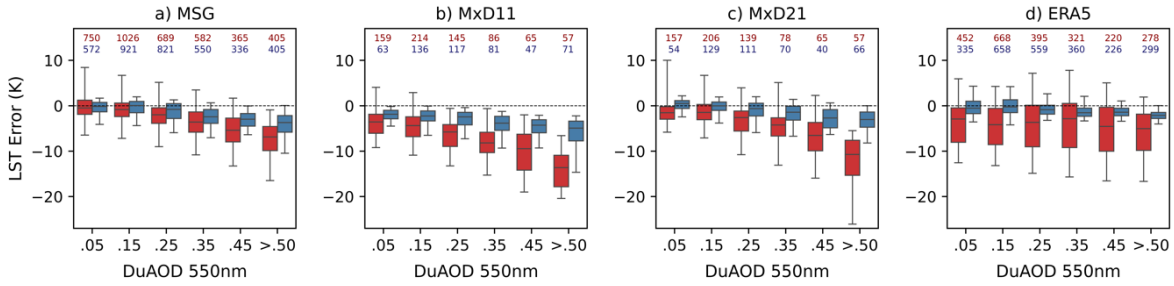

Figure 1.3 — Boxplots of LST Error for six classes of DuAOD comparing in situ LST at the station in Dahra, Senegal, during 2009 to 2013, against: (a) MSG LST; (b) MxD11 LST; (c) MxD21 LST; and (d) ERA5's SKT. Boxes indicate 25th, 50th, and 75th percentiles, and the whiskers the 5th and 95th percentiles. Box coloring reflects daytime (red) and night-time (blue) observations. The x-axis labels indicate the center points of each DuAOD class, except for the last class where the lower bound is indicated. The numbers above each pair of boxes indicate the number of datapoints used in each class, color-coded for time of day. Adapted from [24].

Based on the in situ comparisons, an error of approximately 0.9 °C for every 0.1 increase in DuAOD is estimated for LSA SAF's MSG/SEVIRI LST product. MODIS products show slightly larger median errors and higher dispersion, related to the variable viewing configuration of polar orbiting satellites such as Terra and Aqua: the increased (decreased) atmospheric optical paths for higher (lower) view angles lead to a higher (lower) impact of the aerosols on the retrievals.

Considering that DuAOD values can reach well above 0.5 over the Sahara Desert — reminding that Fig. 1.1 shows season averages and daily values can be much larger — the magnitude of underestimation of LST in that region will, under those conditions, far exceed the 1 °C target accuracy.

1.3 Thesis Research Goals

In this dissertation the underestimation of satellite-based LSTs in conditions of heavy dust aerosol loading is addressed. First, the radiative effect of dust aerosols on satellite-based measurements of surface-emitted TIR radiation is analyzed. This analysis is based on radiative transfer (RT) simulations performed with RTTOV, a fast RT model developed by EUMETSAT's Satellite Application Facility on Numerical Weather Prediction (NWP SAF), using atmospheric profiles and surface variables obtained from the ERA5 and EAC4 reanalyses. Based on the RT analysis, an improvement to the GSW algorithm is explored which accounts for the effect of dust aerosols.

A brief recounting of the history leading to the current state of satellite-based LST retrievals is presented beforehand, which will help introduce general concepts related to the estimation of LST from space.

Chapter 2 — History and General Concepts of Satellite-Based LST Estimations

2.1 Early History of Surface Temperature Estimations in the Thermal Infrared (TIR) Atmospheric Window: 1960s & early 1970s

The launch of the world's first weather satellite — TIROS (Television Infrared Observation Satellite) 1 — in April 1960 revealed, for the first time, the large-scale features of Earth's weather systems as seen from space (Fig. 2.1).

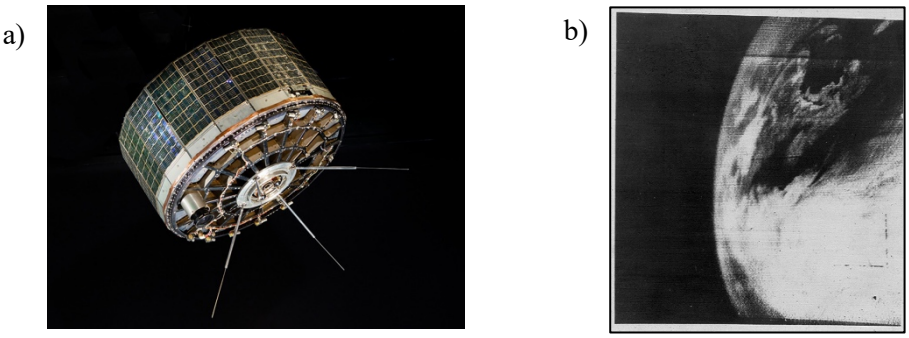

Figure 2.1 — (a) TIROS-1 (credit: https://airandspace.si.edu); (b) One of the first TV images of Earth from space, recorded by TIROS-1 (credit: NASA - http://www.nasa.gov).

While subsequent satellites in the TIROS series were being launched, their exploitation for measuring various meteorological variables was being actively investigated. One of these variables was surface temperature, which can be determined using radiometers sensible to the wavelengths of the TIR atmospheric window (8-12 μm). The atmospheric window is ideal for measuring surface temperature, as it encompasses the peak emission by Earth's surface and has low atmospheric absorption (Fig. 2.2), ensuring a high signal to noise ratio.

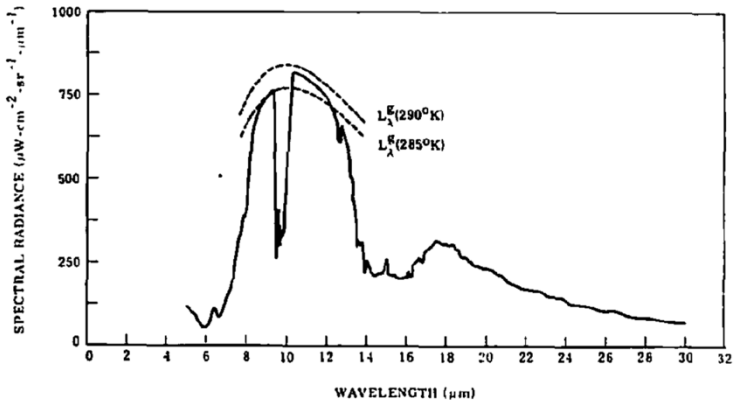

Figure 2.2 — Spectral radiance at 100-km altitude for a water surface temperature of 290 K (solid line). Nadir viewing angle=60°. The two dashed lines represent the radiance of a black body at 290 K and 285 K. If the atmospheric effect is not considered, the sea surface temperature appears to be around 288 K. Adapted from [52].

Soon, some of the main challenges of determining surface temperature from satellite-based measurements were identified, which included accounting for the absorption and emission by water vapor and ozone, the effect of increasing viewing angles, and the issue of cloud-cover [53]. The effect of ozone was easily addressable as it was linearly related to the surface emission and did not have significant seasonal and latitudinal variations. The effect of limb-darkening (the increase in atmospheric absorption due to increasing viewing angles) was corrected using an empirical relation and cloud cover was either identified manually or using measurements of the visible reflected radiation. The effect of water vapor was more complicated to address and a technique that could fully account for it was still several years away.

By 1965 the oceanography community had realized the utility of precise surface temperature measurements for meteorological purposes, such as monitoring storm systems, determining air masses, and identifying fronts [54]. The research on satellite-based SST estimations was further motivated by its utility for commercial activities, such as fishing and transportation, and military operations. However, to achieve high accuracies of SST, it was necessary to address the effect of water vapor. Although this effect could be calculated if the distribution of water vapor in the atmosphere column was exactly known, in the absence of radiosonde observations of humidity only approximate corrections, based on climatological data, were possible [55].

In 1970, a key observation was made by Anding & Kauth [52] which became the foundation for a technique that could efficiently account for the atmospheric effect of water vapor. A linear relationship was found between the satellite-measured radiances of two bands in the atmospheric window (Fig. 2.3). This linearity results from the atmospheric absorption and emission in both bands being small and their relation being well represented by a linear function. Therefore, through two simultaneous radiance measurements in the atmospheric window, the atmospheric effect could essentially be corrected.

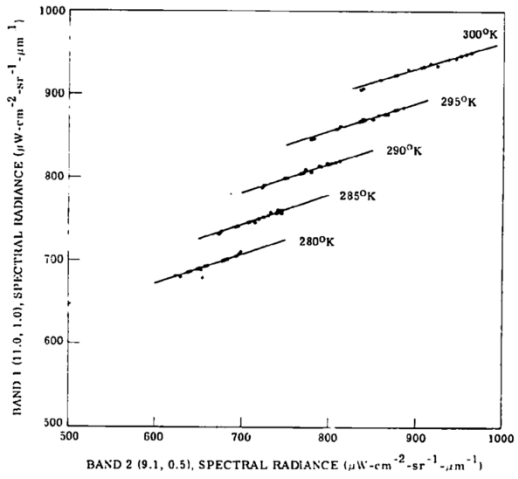

Figure 2.3 — Relation between spectral radiances of two bands in the atmospheric window for various atmospheric states, zenith angles, and SST. For each SST, the radiancies of the two bands for all atmospheric states and zenith angles are linearly related. Adapted from [52].

Although other methodologies for correcting the effect of water vapor were investigated, such as statistically-based methods [58], the use of two window channels to perform the atmospheric correction became a leading technique. A derivation of this approach, termed *split-window*, will be presented after introducing some general concepts of radiative transfer.

2.2 General Concepts of Radiative Transfer

In order to describe the *split-window* approach developed to address the atmospheric attenuation in TIR-based SST retrievals, some general concepts regarding radiative transfer will now be introduced (details may be found in Liou, K. N. (2002) – An Introduction to Atmospheric Radiation [59]).

A pencil of electromagnetic radiation with intensity I_λ (at wavelength λ) traversing a medium is weakened by its interaction with matter through absorption and scattering. The decrease in intensity in a layer with thickness ds of a medium with density ρ is:

$$dI_\lambda = -\,k_\lambda\,\rho\,I_\lambda\,ds \tag{2.1}$$

where k_λ is the mass extinction cross section (in units of area per mass) at λ. "Extinction" refers to absorption and scattering combined.

It follows from Eq. (2.1) that at a point s_1 the intensity is:

$$I_\lambda(s_1) = I_\lambda(s)\cdot\exp\left(-\int_s^{s_1} k_\lambda\,\rho\,ds'\right) \tag{2.2}$$

This defines the monochromatic optical depth:

$$\tau_\lambda(s_1,s) = \int_s^{s_1} k_\lambda\,\rho\,ds' \tag{2.3}$$

represented in Fig. 2.4.

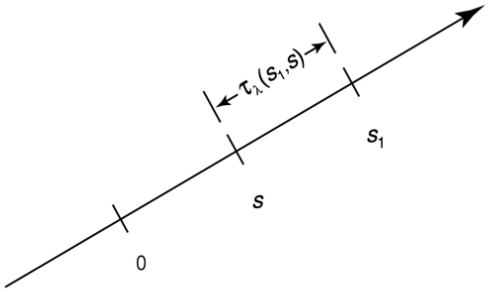

Figure 2.4 — Configuration of the optical depth τ_λ defined in Eq. (2.3). Adapted from [59].

In a homogeneous medium, $\tau_\lambda(s_1,s) = k_\lambda\,u(s_1,s)$, where $u(s_1,s) = \int_s^{s_1}\rho\,ds'$, is the path length. This simplified scenario is referred to as Beer-Bougert-Lambert law:

$$I_\lambda(s_1) = I_\lambda(s)\cdot e^{-k_\lambda\,u(s_1,s)} \tag{2.4}$$

which states that the decrease in intensity caused by a homogeneous medium follows an exponential decay fully determined by the mass extinction cross section, k_λ, and the path length, $u(s_1,s)$.

Returning to the pencil of radiation traversing a medium, in addition to being weakened through absorption and scattering, it can be strengthened by emission from the medium and multiple scattering. The increase in radiation caused by a thickness ds of a given medium is given by:

$$dI_\lambda = j_\lambda \, \rho \, ds \tag{2.5}$$

where j_λ is the source function coefficient (from emission and multiple scattering). Combining both sources of change to the pencil of radiation — the weakening, Eq. (2.1), and the strengthening, Eq. (2.5) — yields the general radiative transfer equation (RTE):

$$dI_\lambda = (-I_\lambda + J_\lambda) \, k_\lambda \, \rho \, ds \tag{2.6}$$

where $J_\lambda \equiv \frac{j_\lambda}{k_\lambda}$ is the source function.

In a medium where scattering can be neglected (which is the case in the TIR range of the spectrum, when no aerosols are present) the source function is equal to the medium's emission, which is given by the Planck function:

$$J_\lambda = B_\lambda(T) \tag{2.7}$$

In this case the RTE can be written as

$$dI_\lambda = (-I_\lambda + B_\lambda[T]) \, d\tau_\lambda \tag{2.8}$$

using $d\tau_\lambda = -\, k_\lambda \, \rho \, ds$, according to the definition of τ_λ.

Integrating Eq. (2.8) over ds from the surface at s=0 to a point s_1, multiplied by the transmissivity $\mathcal{T}_\lambda(s_1, s) = e^{-\tau_\lambda(s_1, s)}$ results in

$$I_\lambda(s_1) = I_\lambda(0) \cdot \mathcal{T}_\lambda(s_1) + \int_0^{s_1} B_\lambda[T(s)] \cdot \mathcal{T}_\lambda(s_1, s) \cdot k_\lambda \rho \, ds \tag{2.9}$$

Considering that s_1 is at the satellite sensor, and writing the integral over $d\mathcal{T}_\lambda$, yields:

$$I_\lambda = I_\lambda(0) \cdot \mathcal{T}_\lambda(p_0) + \int_{\mathcal{T}_\lambda(p_0)}^{1} B_\lambda[T(p)] \cdot d\mathcal{T}_\lambda(p) \tag{2.10}$$

The resulting equation shows that, if scattering is neglected, the radiance measured by the satellite sensor is the sum of the surface-emitted radiance, attenuated by the atmosphere (factored by the transmissivity), and the emission from the various atmospheric layers, which is also attenuated along the way towards the top of the atmosphere (TOA).

2.3 Development of the Split-Window Approach for SST Estimations

In 1972, Prabhakara et al. [60] developed the split-window approach, which could account for the effect of water vapor on SST estimations by measuring the radiance in two adjacent wavelengths in the TIR atmospheric window.

For sea, the emissivity can be approximated to unity and $I_\lambda(0)$ is therefore given by the Planck function for the surface temperature $T(p_0)$. Accordingly, Eq. (2.10) becomes:

$$I_\lambda = B_\lambda[T(p_0)] \cdot \mathcal{T}_\lambda(p_0) + \int_{\mathcal{T}_\lambda(p_0)}^{1} B_\lambda[T(p)] \cdot d\mathcal{T}_\lambda(p) \tag{2.11}$$

Eq. (2.11) can be simplified to

$$I_\lambda = B_\lambda[T(p_0)] \cdot \mathcal{T}_\lambda(p_0) + \bar{B}_\lambda[1 - \mathcal{T}_\lambda(p_0)] \tag{2.12}$$

where $\bar{B}_\lambda$ is the weighted mean Planck emission of the atmosphere $\int_{\mathcal{T}_\lambda(0,p_0)}^{\mathcal{T}_\lambda(0,p)} B_\lambda[T(\mathcal{T})] \cdot d\mathcal{T}_\lambda$ /$[1 - \mathcal{T}_\lambda(p_0)]$.

Additionally, considering that the absorption in the atmospheric window is weak (i.e. k_λ is small), then $\mathcal{T}_\lambda(p_0) = e_\lambda^{-\tau_\lambda(p_0)} = e_\lambda^{-k_\lambda u} \approx 1 - k_\lambda\, u$. Here, u is the effective absorber thickness, equivalent to the path length. Using this approximation for the transmissivity yields:

$$I_\lambda(p) \cong B_\lambda[T(p_0)] - (B_\lambda[T(p_0)] - \bar{B}_\lambda) \cdot k_\lambda\, u \tag{2.13}$$

where $\bar{B}_\lambda = B_\lambda(\bar{T}_\lambda)$, and $\bar{T}_\lambda$ is the equivalent radiative temperature of the atmosphere. Expanding $\bar{B}_\lambda$ and $\bar{T}_\lambda$ in a Taylor series about $T(p_0)$ and keeping only the linear terms we get:

$$\bar{B}_\lambda = B(\bar{T}_\lambda) = B_\lambda[T(p_0)] + \frac{\partial B_\lambda[T(p_0)]}{\partial T}[\bar{T}_\lambda - T(p_0)] \tag{2.14}$$

and I_λ by

$$I_\lambda = B\left[\dot{T}_\lambda\right] = B_\lambda[T(p_0)] + \frac{\partial B_\lambda[T(p_0)]}{\partial T}[\dot{T}_\lambda - T(p_0)] \tag{2.15}$$

where $\dot{T}_\lambda$ is the TOA brightness temperature measured by the satellite sensor at λ. This approximation is valid over a narrow wavelength span and if $\bar{T}_\lambda$ is not strongly dependent on λ, which is the case in the thermal infrared atmospheric window.

Using these two expression in Eq. (2.13) results in a linear relationship between the brightness temperature measured by a satellite sensor and the surface temperature:

$$\dot{T}_\lambda \cong T(p_0) - [T(p_0) - \bar{T}_\lambda] \cdot k_\lambda\, u \tag{2.16}$$

This expression shows that $T(p_0)$ can be determined with a minimum of two measurements in two distinct wavelengths within the window region, λ_1 and λ_2, and with knowledge of the corresponding mass extinction cross sections, k_{λ_1} and k_{λ_2}:

$$T(p_0) = \frac{1}{1 - \frac{k_{\lambda_1}}{k_{\lambda_2}}} \left(\dot{T}_{\lambda_1} - \dot{T}_{\lambda_2} \frac{k_{\lambda_1}}{k_{\lambda_2}} \right) \tag{2.17}$$

Eq. (2.17) shows that the differential absorption in the TIR caused water vapor can be used, due to its linearity, to correct for the atmospheric absorption when estimating surface temperature from satellite-based measurements. This approach, termed split-window, is essentially an approximate inversion of the radiative transfer. The split-window method became widely used for SST retrievals during the 1970s due to its simplicity. Before it can be used for estimations of LST, it must take into account the effect of emissivities, which have a significant contribution to the radiative budget on land surfaces. This leads to the generalized split-window (GSW) algorithm, which is presented next.

2.4 Introduction of the Generalized Split-Window (GSW) Algorithm for LST Estimations

In the late 1980s, the split-window approach started also to be explored for satellite-based estimations of LST [61]–[63]. The estimation of LST poses more challenges than SST. The effect of emissivity is practically negligible for the sea surface, which has an emissivity close to unity, but this is not the case over land surfaces, where emissivities vary considerably amog the different land-surface materials. Additionally, the variation of emissivities with viewing angle is more pronounced for land surfaces than sea, in part due to surface slopes but also, in the case of vegetation, due to the temperature structure of the vegetation canopy [64]. Furthermore, the wider ranges of LST compared to SST, due to lower thermal diffusivity of soil and lower rates of evaporation; the non-uniform field-of-view over land, which can contain surfaces with different temperatures and emissivities; and the larger variation in atmospheric profiles over land compared to sea — all contribute to making LST estimations more challenging than SST [63]. Finally, since the emissivity over land is far from unity, the fraction of downwelling atmospheric emission that is reflected by the surface and reaches the satellite sensor is not negligible and must, therefore, be considered for LST retrievals.

F. Becker (1987) – The Impact of Spectral Emissivity on the Measurement of Land Surface Temperature from a Satellite:

In 1987, F. Becker [62] re-examined the split-window method for land surfaces. The RTE was adjusted to include the effect of emissivity on the surface emission and the contribution of reflected downwelling atmospheric emission, leading to an expression that relates the surface temperature on land, T_s, to the brightness temperature, T_i, retrieved by the satellite sensor:

$$T_s = T_{s_i} - \frac{A_i W (T_a - T_i)}{\varepsilon_i \cos\phi \left(1 - \frac{A_i W}{\cos\phi}\right)} - 2 A_i W \frac{(1 - \varepsilon_i)}{\varepsilon_i} [T_a - T_i - L_i] \tag{2.18}$$

where A_i and W represent, respectively, the atmospheric absorption and the water vapor content of the atmosphere; ϕ is the satellite zenith angle (SZA); ε_i is the emissivity at wavelength λ_i; T_a is the effective air temperature; L_i is a term resulting from the linearization of the Planck function; and T_{s_i} is the surface temperature imposed by T_i and the emissivity ε_i:

$$T_{s_i} = T_i + \frac{1-\varepsilon_i}{\varepsilon_i} L_i \tag{2.19}$$

The first right-hand term in (2.18) is the effect of emissivity on the surface emission, the only term necessary in the absence of an atmosphere (A_i=0); the second right-hand term represents the contribution of absorption and emission by the atmosphere; the third right-hand term is the effect of reflection.

It is possible to combine Eq. (2.18) for each of the two channels i=[1,2]. This eliminates T_a and results in an emissivity-corrected split-window equation:

$$T_s = \frac{T_{s_1} + T_{s_2}}{2} + \frac{T_{s_1} - T_{s_2}}{2} \frac{D_1 + D_2}{D_1 - D_2} - \beta \frac{W A_1 A_2}{D_1 - D_2} \left[\frac{L_1(1-\varepsilon_1)\alpha_2}{\varepsilon_1} - \frac{L_2(1-\varepsilon_2)\alpha_1}{\varepsilon_2} \right] \tag{2.20}$$

where D_i (i=1,2) and β are only dependent on ε_i and/or SZA, A_i and W are atmospheric properties from before, and α_i (i=1,2) are the spectral absorption coefficients of water vapor.

Eq. (2.20) can be reduced, by considering that $(1-\varepsilon)\beta AW \ll \varepsilon$ and $\Delta\varepsilon \ll \varepsilon$, to:

$$T_s = \frac{T_{s_1} + T_{s_2}}{2} + \frac{T_{s_1} - T_{s_2}}{2} \left(\frac{C + 1 + X(C-1)\beta \cos\phi}{C - 1 + X(C+1)\beta \cos\phi} \right) \tag{2.21}$$

where $C = A_2/A_1$ and X is fully defined by ε_i and SZA.

Becker & Li (1990) – Towards a Local Split Window Method over Land Surfaces:

In 1990, Becker and Li [61] introduced a split-window algorithm for LST that could be used in a similar way as that for SST. Since Eq. (2.21) depends only on ε_i and SZA, and not on the atmospheric state, T_s can be expressed as a linear combination of the brightness temperatures of two window channels, T_1 and T_2:

$$T_s = A_0 + P \frac{T_1 + T_2}{2} + M \frac{T_1 - T_2}{2} \tag{2.22}$$

where coefficients A_0, P, and M are defined as follows:

$$A_0 = const.$$

$$P = 1 - p_1(1-\varepsilon)/\varepsilon + p_2 \Delta\varepsilon/\varepsilon^2$$

$$M = m_0 - m_1(1-\varepsilon)/\varepsilon + m_2 \Delta\varepsilon/\varepsilon^2$$

where ε is the average of the two channel emissivities and $\Delta\varepsilon$ is the difference between the emissivities. The values for A_0, p_1, p_2, m_0, m_1, and m_2 can thus be determined by fitting them to a calibration database, which contains simulated data for a variety of atmospheric and surface conditions and the corresponding T_s, T_1, and T_2. Since T_1 and T_2 depend on the spectral response function of the radiometer, coefficients are unique to each sensor. Eq. (2.22) is denoted as *local split-window equation* since the coefficients are dependent on the local emissivity.

Wan, Z. & Dozier, J. (1996) – A Generalized Split-Window Algorithm for Retrieving Land-Surface Temperature from Space:

A refined form of Eq. (2.22) was proposed by Wan and Dozier in 1996 [47], the Generalized Split-Window (GSW) algorithm:

$$T_s = C + \left(A_1 + A_2\frac{1-\varepsilon}{\varepsilon} + A_3\frac{\Delta\varepsilon}{\varepsilon^2}\right)\frac{T_1+T_2}{2} + \left(B_1 + B_2\frac{1-\varepsilon}{\varepsilon} + B_3\frac{\Delta\varepsilon}{\varepsilon^2}\right)\frac{T_1-T_2}{2} \qquad (2.23)$$

Eq. (2.23) has an additional variable coefficient, A_1, allowing the algorithm to be viewing-angle dependent, which Wan and Dozier show to be beneficial. The dependence of the coefficients on atmospheric column water vapor is also suggested to be advantageous.

Presently, GSW is widely used for operational LST retrievals [17] providing estimates with high accuracy (e.g., [18], [22]). In the following section, the LST product by LSA SAF, which is the product that will be attempted to be improved, will be presented.

2.5 The LSA SAF SEVIRI LST Product

The European Organization for the Exploitation of Meteorological Satellites (EUMETSAT) Satellite Application Facility on Land Surface Analysis (LSA SAF) retrieves LST using the Spinning Enhanced Visible and Infrared Imager (SEVIRI) onboard Meteosat Second Generation (MSG) satellites. SEVIRI observes an earth disk with SZA ranging from 0° to 80°, with a temporal resolution of 15 minutes and a spatial resolution of 3 km at nadir.

LSA SAF estimates LST [45] using a GSW algorithm — Eq. (2.23) — as introduced by Wan and Dozier (1996) [46], [47], using SEVIRI brightness temperatures in the channels centered at 10.8 μm, $T_{10.8}$, and 12.0 μm, $T_{12.0}$. Fig. 2.5 shows the spectral response function of both channels for the four satellites in the MSG series.

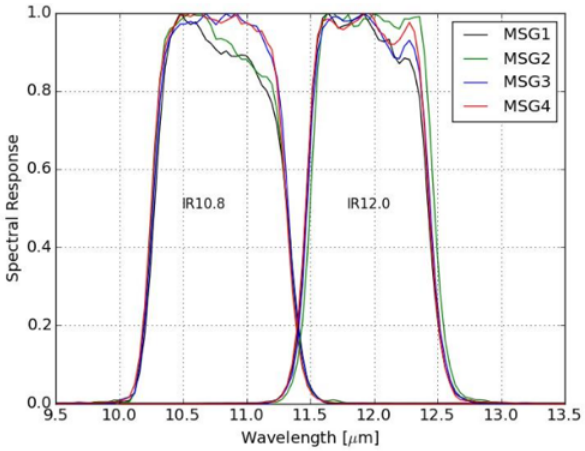

Figure 2.5 — Spectral response of SEVIRI TIR channels, centered at 10.8 and 12.0 μm, onboard MSG1, MSG2, MSG3, and MSG4. Adapted from [65].

LSA SAF's GSW coefficients, A_j, B_j, (j = 1,2,3) and C, are calibrated using a calibration database compiled by Borbas et al. (2005) [66] containing over 15,700 global profiles of temperature, moisture, and ozone that represent a wide range of global (clear-sky) atmospheric conditions. For each condition, the TOA brightness temperatures of the two channels of SEVIRI are simulated using the radiative transfer model MODTRAN4. A fraction of the profiles in the database (77) that cover a broad variety of atmospheric column water vapor are combined with a wide range of surface properties (T_s and ε_i) and used for the calibration of the GSW coefficients. The remaining profiles are used for verification. The coefficients are determined for 8 classes of total column water vapor (TCWV), the maximum being 6 cm, and 16 classes of SZA, up to 75°. Fig. 2.6 shows how each coefficients varies with TCWV and SZA, as well as the explained variance.

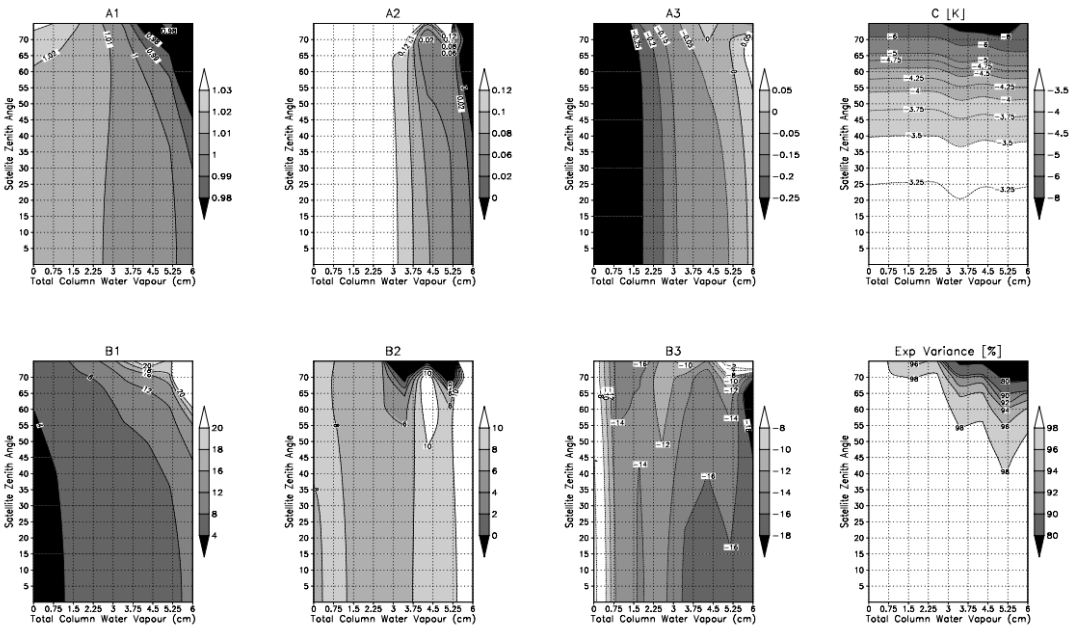

Figure 2.6 — LSA SAF's GSW coefficients and the explained variance (bottom left panel) as a function of SZA and TCWV. Adapted from [65].

Chapter 3 — Analysis of the Radiative Effect of Dust Aerosols on LST Retrievals

An accurate understanding of the effect of dust aerosols on TIR radiation is needed before a methodology to improve LST retrievals in the presence of dust aerosols can be explored. In principle, given the refractive index of dust aerosols [67], [68], some absorption of the surface-emitted TIR radiation will occur as it propagates towards the TOA. In addition, since coarse dust aerosols have sizes comparable to the TIR wavelengths [69], Mie scattering may also play a role in the radiative transfer. Examining how these interactions affect the TIR radiation measured by the satellite sensor is an essential part of this dissertation and relies on simulations using a radiative transfer model (RTM). The RTM chosen for this work is RTTOV, which will be described in the following section with special focus on its capabilities for computing the multiple scattering by aerosols. RTTOV simulations will then be used to investigate how dust aerosols interact with the surface-emitted TIR radiation and how this impacts the estimation of LST from satellite-based measurements.

3.1 RTTOV Fast Radiative Transfer Model

RTTOV (version 13) is a fast RTM currently developed by EUMETSAT's Satellite Application Facility on Numerical Weather Prediction (NWP SAF) [70]. It was originally developed at ECMWF in the early 1990s for use with data acquired by the TIROS Operational Vertical Sounder (TOVS) on-board the TIROS-N/NOAA series of polar-orbiting satellites.

When using RTTOV to simulate the effect of aerosols on TIR measurements, two options are available for computing multiple scattering: using the default RTTOV solver with a Chou-scaling parametrization [71] or the discrete ordinate method (DOM) solver [72]. Using the DOM solver is roughly one or two orders of magnitude computationally more expensive than the default solver with Chou-scaling [73], [74] but should produce more accurate modelling of the multiple scattering. An explanation of the Chou-scaling parametrization (3.1.1) and the DOM solver (3.1.2) will be presented next.

3.1.1 Chou-scaling Parametrization

(Based on [71], [75]*)*

The basic principle of the Chou-scaling is to decrease the optical depth, τ, and therefore increase the transmission, $\mathcal{T}$, such that the contribution of upward backscattering by the aerosols of downwelling atmospheric radiation is incorporated in the atmospheric emission term.

Before deriving the Chou-scaling parametrization, it is necessary to introduce the extinction coefficient, β_e. This coefficient determines the amount of energy removed from a pencil of radiation through extinction, i.e., through absorption and scattering. The extinction coefficient is thus the sum of the absorption, β_a, and scattering, β_s, coefficients and the units are given in terms of length (cm^{-1}). A useful quantity in radiative transfer is the single-scattering albedo, $\bar{\omega}$, defined as:

$$\bar{\omega} = \frac{\beta_s}{\beta_e} \tag{3.1}$$

The derivation of the Chou-scaling parametrization starts by defining the apparent emission, $dI'(\tau, \mu)$, of a layer with thickness $d\tau$ in the zenithal direction μ. μ is related to zenithal angle θ (Fig. 3.1) through μ=cos θ.

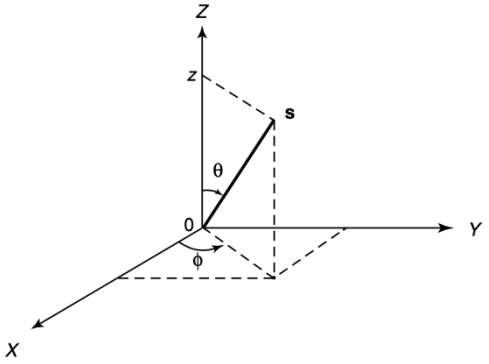

Figure 3.1 — Geometry of a plane-parallel atmosphere, where s is the position vector and θ and ϕ denote the zenith and azimuthal angles, respectively. Adapted from [59].

The apparent emission, $dI'(\tau, \mu)$, is thus the sum of the radiance emitted and the radiance reflected (i.e. backscattered) by the layer $d\tau$ in the direction μ:

$$dI'(\tau, \mu) = \frac{d\tau}{\mu}\frac{\bar{\omega}}{2}\int_{-1}^{0} I(\tau, \mu')\, \mathcal{P}(\mu, \mu')\, d\mu' + (1 - \bar{\omega})B[T(\tau)]\frac{d\tau}{\mu} \tag{3.2}$$

where μ' is the cosine of the zenith angle of incoming radiation, $I(\tau, \mu')$ is the diffuse radiance field, $\mathcal{P}$ is the phase function (which describes the angular distribution of the energy scattered by a particle), and $B[T(\tau)]$ is the Planck function at temperature $T(\tau)$.

As described by Eq. (3.2), $dI'(\tau, \mu)$ has two contributions:

i. The upward scattering of downwelling atmospheric radiation caused by the layer $d\tau$, represented by the first right-hand term. The limits of integration are [-1,0] which restricts the incoming diffuse radiation, $I(\tau, \mu')$, to only the downwelling contribution, since μ'=cos θ' and thus μ'=[-1,0] $\Longrightarrow$ θ'=[$\frac{\pi}{2}$, $\frac{3\pi}{2}$];

ii. The emission by the layer $d\tau$, represented by the second right-hand term. This term is determined by the temperature of the layer, $T(\tau)$, and $\bar{\omega}$.

In the case of $\bar{\omega}$=0, i.e. a medium which does not scatter and only absorbs, then $dI'(\tau, \mu)$ is the real emission of the layer (second right-hand term). If $\bar{\omega}$=1, i.e. a medium which only scatters and does not absorb, then the apparent emission would be entirely given by the backscattering (first right-hand term). It is important to notice that the optical depth, τ, is used here as a vertical coordinate. This is only possible when considering a plane-parallel atmosphere and distances are measured normal to the plane of stratification.

By assuming that the diffuse radiance field, $I(\tau, \mu')$, is isotropic and can be approximated by $B[T(\tau)]$, it is possible to rewrite the expression for $dI'(\tau, \mu)$ as

$$dI'(\tau,\mu) = [1 - \bar{\omega}(1-b)] \cdot B[T(\tau)] \frac{d\tau}{\mu} \tag{3.3}$$

where b is the integrated fraction of energy scattered backwards (μ=[0,1]) for incident radiation from above (μ'=[-1,0]):

$$b = \frac{1}{2}\int_0^1 d\mu \int_{-1}^0 \mathcal{P}(\mu,\mu')\, d\mu' \tag{3.4}$$

The last step in for the Chou-scaling parametrization is to approximate the apparent optical depth of the layer, $d\tilde{\tau}$, by:

$$d\tilde{\tau} = d\tau_a + b\, d\tau_s \tag{3.5}$$

where $d\tau_a$ is the component due to absorption by the medium and the second right-hand term represents the contribution to the apparent optical depth of the backscattering. Since the backscattering increases the apparent transmissivity of the medium, $d\tau_s$ must be negative, resulting in $d\tilde{\tau}$ being smaller than $d\tau$. This becomes clear by rewriting Eq. (3.5), using $\bar{\omega} = \frac{d\tau_s}{d\tau}$:

$$d\tilde{\tau} = [1 - \bar{\omega}(1-b)]\, d\tau \tag{3.6}$$

Substitution Eq. (3.5) in Eq. (3.3) yields:

$$dI'(\tau,\mu) = B[T(\tau)] \frac{d\tilde{\tau}}{\mu} \tag{3.7}$$

In essence, since $d\tilde{\tau} < d\tau$, the Chou-scaling parametrization reduces the optical depth (increases the transmissivity of the medium), so that the contribution of upward backscattered downwelling atmospheric radiation is accounted for in the atmospheric emission term.

By introducing the term given by Eq. (3.7) into the RTE, calculations with multiple scattering will not differ significantly from clear-sky simulations and are, therefore, computationally efficient. It is important to note, however, that the approximation of diffuse radiance field, $I(\tau,\mu')$, by the Planck function will have a small effect on accuracies of radiances. Theses inaccuracies were assessed by Matricardi (2005) [71] and found to be less than 1 K for simulations of multiple scattering by dust aerosols in the thermal infrared.

3.1.2 Discrete Ordinates Method (DOM)

(Based on [72], [76]–[78]*)*

A completely distinct method to the Chou-scaling parametrization, which simplifies the computationally intensive operation of calculating the multiple scattering by aerosols, is the discrete ordinates method (DOM). In this case, the full RTE is solved, including the term for multiple scattering. The fundamental approach of DOM is to subdivide the directions of scattering of radiation into a discrete amount of

zenithal directions μ_i — the ordinates — and representing the radiance field by a series of Fourier modes, $I^m(\tau, \mu)$, which transforms the integro-differential equation into a matrix multiplication problem.

Assuming a plane-parallel approximation, the RTE in the IR (i.e., without the component of primary-scattering of solar radiation) is given by:

$$\mu \frac{dI(\tau, \mu, \varphi)}{d\tau} = I(\tau, \mu, \varphi) - \frac{\omega_0}{4\pi} \int_0^{2\pi} \int_{-1}^{1} \mathcal{P}(\cos\Theta)\, I(\tau, \mu', \varphi') d\mu' d\varphi' - (1 - \omega_0) B(\tau) \qquad (3.8)$$

where Θ is the scattering angle between (μ, φ) and (μ', φ') — φ (φ') is the azimuthal angle (see Fig. 3.1) of outgoing (incoming) radiation.

Eq. (3.8) is easily interpretable: the variation in outgoing radiance, $dI(\tau, \mu, \varphi)$, in the direction (μ, φ), caused by a layer with thickness $d\tau$, at a given height τ, is determined by:

(i) The outgoing radiance from the layer immediately below, $I(\tau, \mu, \varphi)$;
(ii) The radiance due to multiple scattering, represented by the second right-hand term. The incoming diffuse radiance, $I(\tau, \mu', \varphi')$, is multiplied by the phase function, $\mathcal{P}$, which describes the angular distribution of the energy scattered. This is integrated over all zenithal and azimuthal directions;
(iii) The emission of the layer, given by the Planck function for the temperature of the atmosphere at τ, considering the single scattering albedo of the atmosphere, ω_0.

In order to solve Eq. (3.8) numerically, the phase function, $\mathcal{P}$, which does not have a simple mathematical description, as it is not possible to represent the scattering of radiation by a medium filled with various types and sizes of particles through an equation, must be represented by an infinite series of Legendre polynomials $P_l(\cos\Theta)$:

$$\mathcal{P}(\cos\Theta) = \sum_{l=0}^{\infty} p_l P_l(\cos\Theta) \qquad (3.9)$$

Through various considerations, which are not going to be presented here, it is possible to arrive at a description of $\mathcal{P}$ where the (μ, μ')-dependence has been completely separated from the (φ, φ')-dependence:

$$\mathcal{P}(\cos\Theta) = \sum_{m=0}^{\infty} (2 - \delta_{0m}) \sum_{l=m}^{\infty} p_l^m P_l^m(\mu) P_l^m(\mu') \cos m(\varphi - \varphi') = \mathcal{P}(\mu, \varphi, \mu', \varphi') \qquad (3.10)$$

This is useful, as this will allow the RTE to be discretized in the zenithal direction (μ_i), without needing to discretize the azimuthal direction. The same is required for the radiance field, $I(\tau, \mu, \varphi)$, which can be expressed by means of a Fourier series, where the m-th Fourier mode of the radiance, $I^m(\tau, \mu)$, is only dependent on μ:

$$I(\tau, \mu, \varphi) = \sum_{m=0}^{\infty} (2 - \delta_{0m}) I^m(\tau, \mu) \cos m\varphi \qquad (3.11)$$

Inserting Eq. (3.10) and Eq. (3.11) into Eq. (3.8), and following additional intermediate steps, it is possible to arrive at a RTE for $I^m(\tau, \mu)$:

$$\mu \frac{dI^m(\tau,\mu)}{d\tau} = I^m(\tau,\mu) - \frac{\omega_0}{2} \int_{-1}^{1} \sum_{l=m}^{\infty} p_l^m P_l^m(\mu) P_l^m(\mu') I^m(\tau,\mu') d\mu' - (1-\omega_0) B(\tau) \delta_{0m} \quad (3.12)$$

where δ_{0m} is a Kronecker delta.

Two issues must still be addressed in order to solve the full RTE and both are related to the discretization of μ_i: Firstly, Eq. (3.12) is valid for an arbitrary direction μ, which would result in an infinite system of equations to solve the RTE; Secondly, the second right-hand term of Eq. (3.12) must be discretized in order to be numerically computable. The solution introduced by the DOM method is to:

(i) Approximate the multiple scattering integral with the help of the Gaussian quadrature:

$$\int_{-1}^{1} f(\mu)\, d\mu \approx \sum_{i=1}^{r} w_i f(\mu_i) \quad (3.13)$$

where w_i are the weights and μ_i are the roots of the Legendre polynomials $P_r(\mu)$.

(ii) Discretize the continuous zenithal angles into 2s directions, denoted streams, as represented in Fig. 3.2(a). The choice of these streams is such that they do not cluster near μ=1 and μ=-1. This would be an issue for strongly anisotropic phase functions, as the accuracy of the radiance field would not improve significantly by simply increasing the number of nodes. By using the scheme of streams shown in Fig. 3.2(b), streams are not only clustered in both the upward and downward directions but also near the horizon.

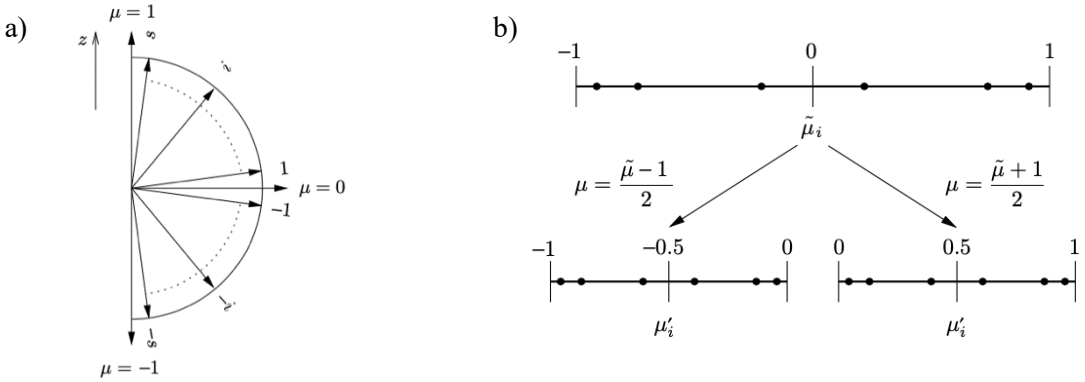

Figure 3.2 — Discretization of $I(\tau,\mu_i)$ into 2s directions (streams). (b) Distribution of streams known as double-Gaussian quadrature rule. The dots mark the quadrature nodes i = 1,…,s. Adapted from [76]

In this way, for each $I^m(\tau,\mu_i)$, the multiple scattering term is calculated for 2s discrete directions between μ=1 and μ=–1. This process is repeated for each of the 2s μ_i. As an example, Eq. (3.12) is evaluated for m=0 (analogously for m≠0) for the discrete direction μ_i:

$$\mu_i \frac{dI(\tau,\mu_i)}{d\tau} = I(\tau,\mu_i) - \frac{\omega_0}{2} \sum_{j=-s}^{s} w_j\, I(\tau,\mu_j)\, \mathcal{P}(\mu_i,\mu_j) - (1-\omega_0) B(\tau) \quad (3.14)$$

where $\mathcal{P}(\mu,\mu') = \sum_{l=0}^{\infty} p_l^m P_l^m(\mu) P_l^m(\mu')$ is introduced to simplify notation.

By separating the upwelling and downwelling contributions, Eq. (3.14) can be written in a vector-matrix form which can then be transformed into an eigenvalue problem. This results in the following solution of the (azimuthally averaged) RTE for a homogeneous layer:

$$I(\tau, \mu_i) = \sum_{j=-s}^{s} D_j \, F_j(\mu_i) \exp(-k_j \tau) + Z(\mu_i) \exp\left(-\frac{\tau}{\mu_0}\right) \tag{3.15}$$

where D_j are constants, obtainable from the boundary conditions at the upper and lower boundary of the homogeneous layer, $F_j(\mu_i)$ is the i-th component of the j-th eigenvector, k_j is the eigenvalue, and $Z(\mu_i)$ are coefficients that can be determined from Eq. (3.8).

Eq. (3.15) is the solution for a single homogeneous layer. To solve it for the entire (inhomogeneous) atmosphere, the atmosphere can be subdivided into Q different homogeneous sublayers q, resulting in a total of 2sQ equations. The integration constants, $D_{q,j}$, are given by the specifications of the boundary conditions at the top of the atmosphere and at the surface and the remaining, as well as by the requirement that the radiance for each μ_i must be continuous at interface between each layer. This requirement yields a linear equation system that can be written in matrix form and solved by numerical inversion to obtain the values for $D_{q,j}$. In this way, the DOM approach transforms the difficult problem of solving the integro-differential RTE equation into a matrix multiplication exercise.

3.2 RTTOV Simulations of the Radiative Effect of Dust Aerosols in the Thermal Infrared

3.2.1 Data and Study Area

Input data for the RTTOV simulations is obtained from ECMWF's fifth-generation climate reanalysis, ERA5 [79], and CAMS' global reanalysis, EAC4 [80], which is optimized to estimate atmospheric composition. ERA5 is used to obtain surface variables, namely 2-m temperature (T2m), skin temperature (Tskin), surface pressure (SP), and vertically integrated variables, namely total cloud cover (TCC) and total column water vapor (TCWV). EAC4 is used to obtain atmospheric profiles, namely humidity (q), temperature (t), and profiles of dust aerosol mixing ratio, which come in three aerosol size ranges: 0.03-0.55 µm (aermr04), 0.55-0.9 µm (aermr05), and 0.9-20 µm (aermr06). Additionally, dust aerosol optical depth at 550 nm (DuAOD) from EAC4 is also used. All profiles are obtained at the 60 EAC4 model levels and all variables are interpolated to a 1° x 1° spatial grid. To be compatible with EAC4's time sampling, ERA5 data are selected in three-hourly time steps. Only land and clear-sky conditions are considered here, which is ensured by limiting TCC to values below 30%. Data are obtained for the year 2019 across the area delimited by the rectangle in Fig. 3.3, which restricts this analysis to the Sahara Desert. This data is used as input to the RTTOV simulations, assigning the same emissivity (ε=0.96) to both SEVIRI channels in order to eliminate the effect emissivities from the analysis of the radiative effect of the aerosols.

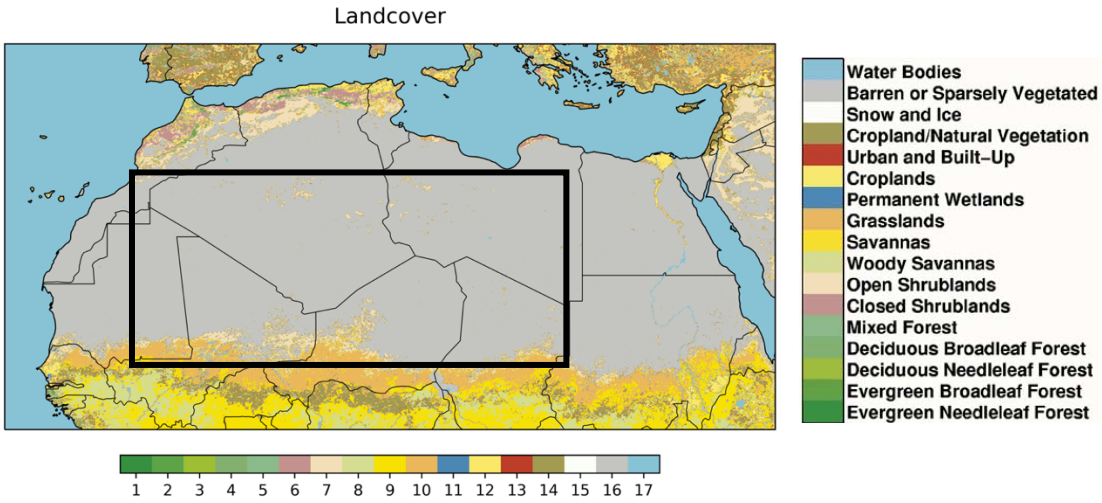

Figure 3.3 — Area delimited by rectangle indicates ERA5 and EAC4 data selected for year 2019, with landcover types by [81].

3.2.2 RTTOV Simulations using Chou-scaling vs DOM

Before starting the analysis of the effect of dust aerosols on surface-emitted TIR radiation, the two methods available in RTTOV for simulating multiple scattering by aerosols— the DOM solver and the Chou-scaling parametrization — are compared. This is done by examining the simulated TOA brightness temperatures (BTs) produced by both methods for the SEVIRI channel centered at 10.8 and 12.0 µm. Simulations are performed with and without aerosols for both schemes. Fig. 3.4 shows the differences between DOM and Chou BTs as a function of TCWV (Fig. 3.4(a)) and DuAOD (Fig. 3.4(b)). Non-negligible differences exist between BTs simulated by the two methods, DOM BTs having higher values than Chou, irrespective of whether aerosols are included in the simulations. Differences range between 1 °C and 2 °C for low TCWV but decrease with increased water vapor content. When dust aerosols are included in the simulations, the DOM-Chou differences also decrease with increasing aerosol concentrations, as shown in Fig. 3.4(b). Notably, the simulations with large values of DuAOD can be found in Fig. 3.4(a) around TCWV=10kg/m^2.

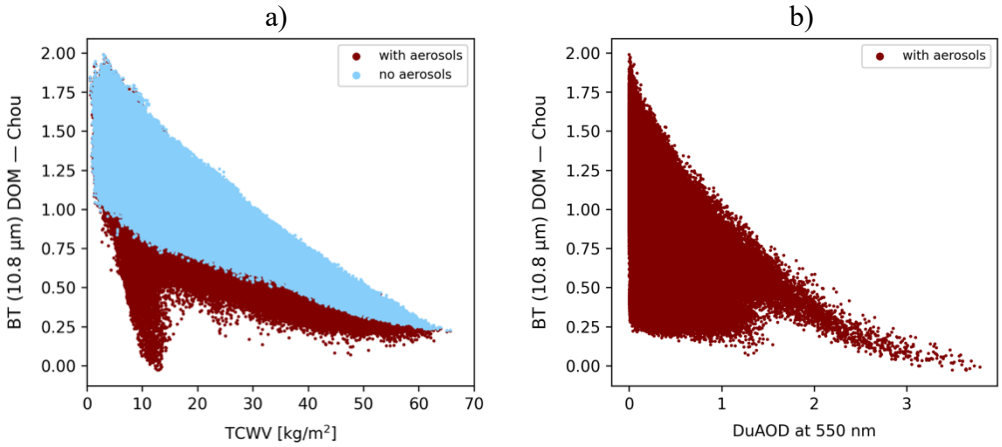

Figure 3.4 — Differences in BT between RTTOV simulations using DOM solver and Chou-scaling parametrization for the SEVIRI channel centered at 10.8 µm as a function of: (a) TCWV and (b) DuAOD. Simulations are performed with (red) and without (blue) aerosol profiles as input. Note that the blue dots of panel (a) cover red dots.

The large differences between Dom and Chou exist whether aerosols are included in the simulations or not, therefore, the observed biases are not caused by the computation of multiple scattering. These differences result from a limitation of RTTOV in representing the variation of optical properties across the channels which leads to errors when using the DOM solver, given that this is a solver for monochromatic radiances [70], [72]. In other words, errors using DOM in the infrared are usually dominated by limitations in simulating gas absorption. However, as the amount of scattering material increases, scattering becomes more dominant than absorption, reducing the impact of those errors on the BTs.

This shortcoming of the DOM solver is corroborated by comparisons of DOM and Chou BTs against BTs obtained with MODTRAN, a different RTM with higher accuracy, using a smaller set of simulations. As shown in Fig. 3.5, Chou BTs are close to MODTRAN BTs, while DOM biases against MODTRAN are similar to DOM biases against Chou (from Fig. 3.4).

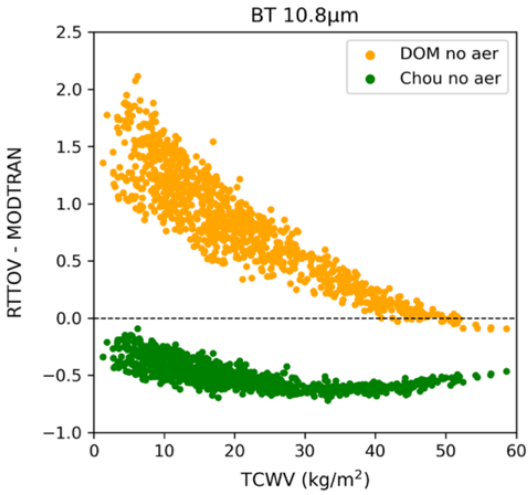

Figure 3.5 — Comparison of BTs simulated with RTTOV (DOM and Chou) against MODTRAN for the SEVIRI channel centered at 10.8 µm. Simulations are performed without aerosols.

Nevertheless, the DOM solver is expected to provide better simulations of the scattering effects than the Chou-scaling [73], [74], [82]. In the calibration of the GSW, it is important that both water vapor and aerosol atmospheric effects are correctly represented in the simulation data. Therefore, in the calibration of the GSW, the Chou-scaling simulations without aerosols are taken as the reference for the general representation of the clear-sky BT, and the DOM solver is used to introduce the BT shift due to the aerosol effects, i.e.:

$$BT_{TOA_{aer}} = BT_{Chou_{noaer}} + \left(BT_{DOM_{aer}} - BT_{DOM_{noaer}}\right) \tag{3.16}$$

where $BT_{Chou_{noaer}}$ is the TOA BT from Chou simulations without aerosols, $BT_{DOM_{aer}}$ is the TOA BT from DOM simulations with aerosols, and $BT_{DOM_{noaer}}$ is the TOA BT from DOM simulations without aerosols .

3.2.3 Analysis of the Impact of Dust Aerosols on TIR Radiation

To analyze the radiative effect of dust aerosols on TIR-based LST retrievals, in particular those employing a GSW algorithm, it is first important to examine the differences in BT between the two channels used for the split-window approach. The BT difference is one of the main inputs in the GSW algorithm (Eq. (2.23)) and is an essential parameter for the atmospheric correction performed by the algorithm. Analyzing its behavior when concentrations of dust aerosols are high can give key insights into the cause of LST underestimation. Since RTTOV simulations are performed for the SEVIRI channels (centered at 10.8 and 12.0 µm), BT differences are given by:

$$\text{BT difference} = BT_{10.8} - BT_{12.0} \tag{3.17}$$

Fig. 3.6 shows BT differences simulated with RTTOV as a function of TCWV and DuAOD (Fig. 3.6(a)) alongside BT differences based on SEVIRI radiances measured over the Sahara Desert for the period 2009-2013 [24] (Fig. 3.6(b)). Results from RTTOV simulations are similar to SEVIRI measurements. Some differences are expected since the RTTOV simulations presented here were performed with equal emissivities for both channels, while desert emissivities typically have larger values at 12.0 than 10.8 µm, which contributes to the BT differences provided by the satellite measurements. In both cases, BT differences increase with TCWV, a well-known behavior in the TIR window [17] which is exploited by the GSW to perform the atmospheric correction during LST retrievals. Similarity also exists in the dependence of the BT differences with DuAOD: in contrast to water vapor, BT differences tend to decrease with increasing concentrations of dust aerosols, a behavior that has already been shown in previous studies [29], [32], [35], [41].

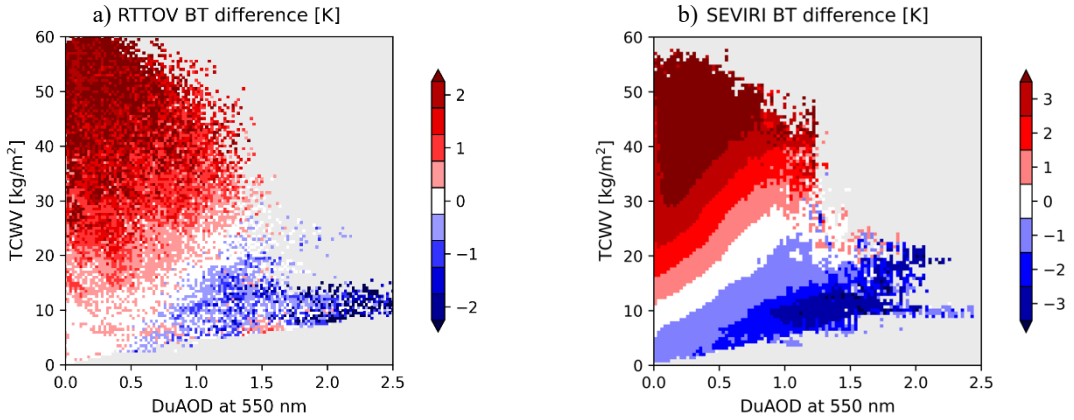

Figure 3.6 — BT differences of SEVIRI TIR channels (as 10.8 µm minus 12.0 µm) as a function of TCWV and DuAOD: (a) simulated with RTTOV; (b) observed by SEVIRI (adapted from [24]).

This opposite behavior of BT differences with DuAOD compared to TCWV is the main driver of the underestimation of LST by the GSW algorithm when dust aerosol concentrations are high. In aerosol-free conditions, absorption of surface-emitted radiation by atmospheric water vapor is higher at 12.0 µm than at 10.8 µm, resulting in the increase in BT difference shown in Fig. 3.6. Therefore, the measured BT difference provides the algorithm with essential information for the correction of the effects of water vapor. However, when dust aerosols are present, the measured BT differences are lower than they would be if the atmosphere were aerosol-free, resulting in an underestimation of actual surface emission and,

thus, an underestimation of LST. This issue is further exacerbated when TCWV and DuAOD are moderate-to-high, because, in such conditions, the total atmospheric absorption of the surface-emitted TIR radiation is the combination of absorption by water vapor and by dust aerosols. However, because BT differences are lower than expected (due to DuAOD), the GSW only partly accounts for the absorption by water vapor. The errors are further amplified by the absorption by the dust aerosols, which is not represented in the algorithm. This combination of circumstances causes the extreme underestimations of LST observed in Dahra, Senegal over –10 K [24].

The variation of BT differences with increasing dust aerosol concentrations is consistent with the optical properties of this type of aerosols: the imaginary part of its complex index of refraction is higher at 10.8 µm than at 12.0 µm [67], [68], i.e. an atmosphere with heavy dust aerosol loading will have a lower transmissivity in the 10.8 µm channel, resulting in progressively more negative BT difference with increased dust aerosol concentration. This effect can be clearly seen in Fig. 3.7, where the variation in transmissivity simulated by RTTOV for both SEVIRI TIR channels is shown as a function of DuAOD (and TCWV). Transmissivity of the 10.8 µm channel is more affected by dust aerosols than the 12.0 µm channel, which is reflected by the slopes of the transmissivity isolines that are strongly negative with DuAOD for channel 10.8 µm and flatter for channel 12.0 µm. As an example, for TCWV=10 kg/m^2, the transmissivity of channel 10.8 µm decreases by 0.3 over 2 units of DuAOD, while in channel 12.0 µm the transmissivity only decreases by 0.2 over the same 2 units of DuAOD. This *differential absorption* caused by dust aerosols in the TIR window is similar to that observed for water vapor, although in the opposite direction. This can be seen in Fig. 3.7, where the decrease in transmissivity with TCWV is more pronounced in the 12.0 µm channel compared to the 10.8 µm channel. For example, transmissivity in the 12.0 µm decreases to 0.4 at TCWV=45 kg/m^2, while at 10.8 µm this only occurs at TCWV=55 kg/m^2.

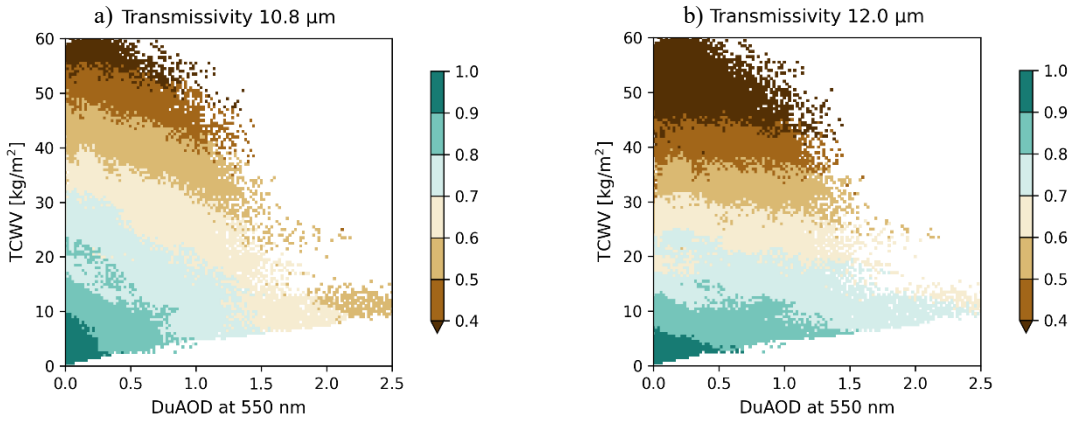

Figure 3.7 — Atmospheric transmissivity as a function of TCWV and DuAOD simulated with RTTOV for the two SEVIRI TIR channels: (a) 10.8 µm; (b): 12.0 µm.

The decrease in transmissivity with DuAOD shown in Fig. 3.7 indicates that less surface-emitted radiance reaches the TOA when TIR-absorbing dust aerosols are present. Conversely, due to the absorption by dust aerosols, the atmospheric emission should also increase when these aerosols are present, causing an increase in atmospheric-emitted radiance reaching the TOA. To evaluate the relative magnitudes of increased atmospheric absorption and emission, first the difference in total radiance reaching the TOA caused by dust aerosols is examined. Fig. 3.8 shows the delta in TOA radiances between simulations with and without aerosols, as a function of DuAOD (and TCWV) for both SEVIRI TIR channels. The total radiance at the TOA is found to decrease due to the presence of dust aerosols

and this deficit becomes more pronounced with increasing DuAOD. This effect is stronger in channel 10.8 than in channel 12.0, as expected given the impact of dust aerosols on transmissivity (Fig. 3.7).

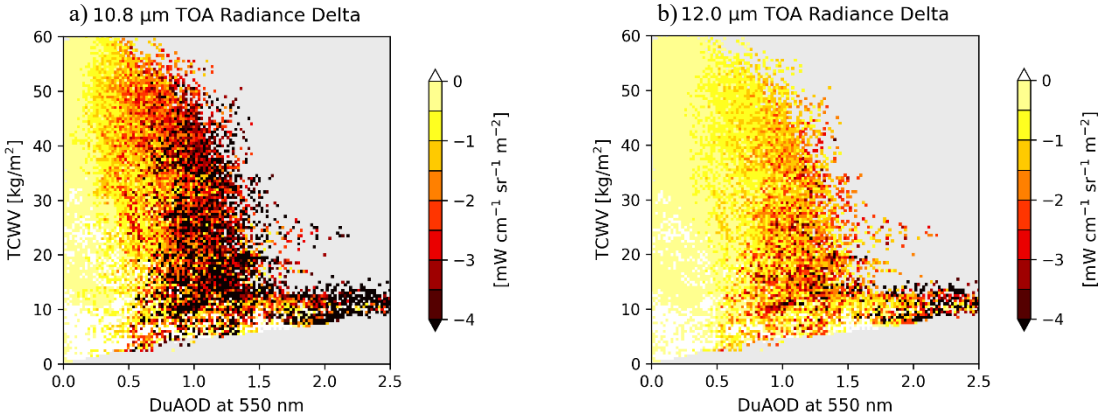

Figure 3.8 — Difference in TOA Radiance caused by dust aerosols as a function of TCWV and DuAOD simulated with RTTOV for the two SEVIRI TIR channels: (a) 10.8 µm; (b): 12.0 µm.

Assuming that TOA radiances usually have values in the order of 100 $mW\ cm^{-1}\ sr^{-1}\ m^{-2}$ and using rough estimates of delta values from Fig. 3.8, for very high values of DuAOD (around 2.0) TOA radiances can decrease by roughly 4%, which is not substantial given that transmissivity decreases by as much as 40% for such DuAOD values. This suggests that much of the absorption of surface-emitted radiation by dust aerosols is compensated at TOA by an increase in atmospheric emission caused by those same aerosols. Indeed, when looking at the differences in atmospheric emission reaching the TOA due to dust aerosols (Fig. 3.9) an increase of roughly 6 times (~ 25 $mW\ cm^{-1}\ sr^{-1}\ m^{-2}$ for channel 10.8 µm at DuAOD=2.0) can be observed compared to the largest deficit in total TOA radiance (~ –4 $mW\ cm^{-1}\ sr^{-1}\ m^{-2}$) . This means that, by simply considering the budget of energy at TOA, a decrease of roughly 30 $mW\ cm^{-1}\ sr^{-1}\ m^{-2}$ in surface-emitted radiance reaching the TOA is to be expected for DuAOD=2.0. This is exactly what is shown by the values of surface emission reaching the TOA (Fig. 3.10), which reduce by about 30 $mW\ cm^{-1}\ sr^{-1}\ m^{-2}$. RTTOV does not output the contribution by backscattered radiation to TOA radiances, however, the considered radiance budget suggests that the contribution of backscattering is not significant.

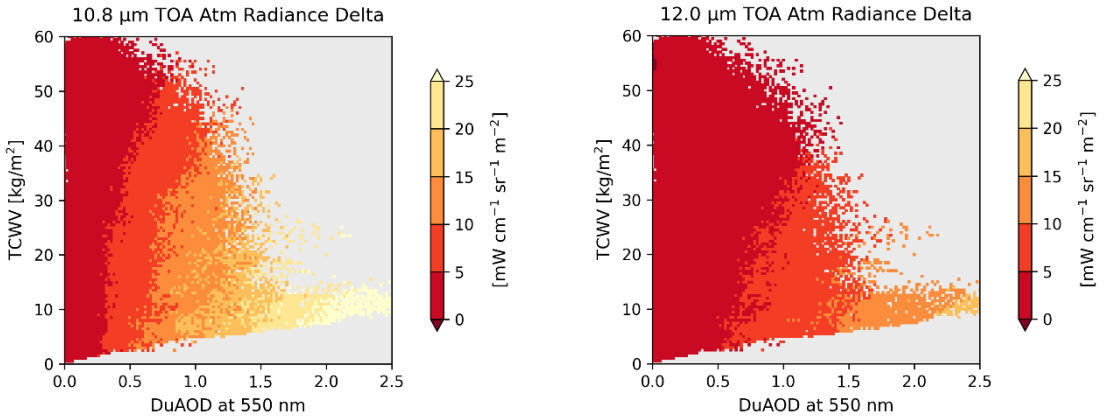

Figure 3.9 — Difference in atmospheric emission reaching the TOA caused by dust aerosols as a function of TCWV and DuAOD simulated with RTTOV for the two SEVIRI TIR channels: (a) 10.8 µm; (b): 12.0 µm.

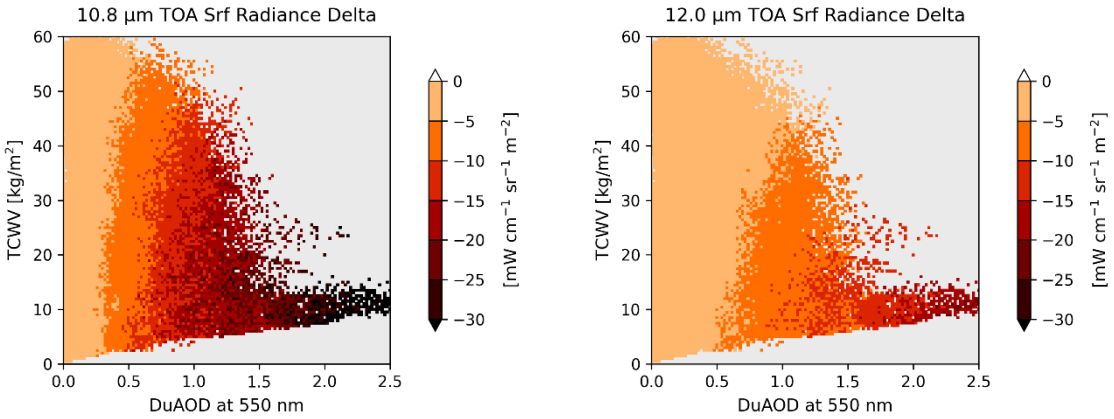

Figure 3.10 — Difference in surface emission reaching the TOA caused by dust aerosols as a function of TCWV and DuAOD simulated with RTTOV for the two SEVIRI TIR channels: (a) 10.8 µm; (b): 12.0 µm.

The results presented in this section, especially on the differential absorption by dust aerosols, give a promising outlook for addressing the effect of dust aerosols with a new calibration of the GSW algorithm, since the split-window approach is specifically designed to exploit differential absorption and correct for the attenuation in the atmosphere. On this basis, an aerosol-robust GSW algorithm is explored in the next chapter.

Chapter 4 — Aerosol-Robust LST Retrievals

Having established that dust aerosols cause differential absorption of the surface-emitted TIR radiation, one possible approach for improving the accuracy of LST retrievals using the GSW algorithm under moderate-to-high dust aerosol concentrations is to calibrate DuAOD-dependent GSW coefficients, given the characteristic ability of the split-window technique to exploit differential absorption and account for atmospheric attenuation. In order to calibrate a DuAOD-dependent GSW, a calibration database which represents a broad range of atmospheric and surface conditions for various DuAOD ranges is required. The method used for constructing such a database is introduced next (Section 4.1), followed by an examination of the database produced (Section 4.2). This database is then used to calibrate a DuAOD-dependent GSW algorithm (Section 4.3), whose performance is then assessed (Section 4.4).

4.1 Profile Selection Methodology for a DuAOD-dependent GSW Calibration Database

A GSW calibration database must represent a wide range of atmospheric and surface conditions to ensure the robustness of the algorithm over all possible scenarios. For a DuAOD-dependent GSW algorithm, the calibration database must have a good representation of atmospheric and surface conditions likely to occur at various classes of DuAOD. The data used to build this database is from ERA5 and EAC4, as described in Section 3.2.1., except that here data for the entire globe over the period 2019–2021 are used. To perform the selection of a set of representative conditions from a pool of data the methodology first introduced by Chevallier et al. (2000) [83] is adopted, which allows to select the N most dissimilar conditions within a given class of atmospheric and surface conditions. The process for creating this DuAOD-dependent calibration database follows the approach by Ermida & Trigo (2022) [84].

The entire pool of data — containing surface variables and profiles of temperature (t), humidity (q), and dust aerosol mixing ratio ($aermr04$, $aermr05$, and $aermr06$ – corresponding to the three aerosol size ranges) for the entire globe between 2019 and 2021 — is first subdivided into classes of TCWV varying from 0 to 60 mm in steps of 5 mm and classes of Tskin varying from 190 to 350 K in steps of 10 K. Additionally, the data is subdivided into DuAOD classes with boundary values 0.05, 0.1, 0.2, 0.4, 0.6, and 0.8. These boundaries were chosen to guarantee a good distribution of data within each class. For values of DuAOD higher than 0.8 the sample of data is not large enough using only three years of data. Subdividing the data into classes of DuAOD, TCWV, and Tskin, ensures that all surface conditions for each bulk atmospheric condition is represented. Note that only "clear-sky" conditions are considered here (i.e., profiles where TCC is below 30%) and only from locations with elevations below 2000 m. The latter requirement is introduced to ensure the variability between profiles is mainly due to different atmospheric conditions and restrict the effect of elevation.

Next, from each subset (i.e. for a given class of DuAOD, TCWV, and Tskin) approximately N=500 conditions are selected using the dissimilarity methodology of Chevallier et al. (2000) [83]. (Larger values of N did not show significant increase in representativeness of the conditions selected and therefore N=500 is used). The dissimilarity between two profiles, i and j, of a given variable, var, is measured by their distance:

$$D_{var}(i,j) = \left\{ \sum_{k=1}^{60} \left(\frac{var_i(k) - var_j(k)}{\sigma_{var}(k)} \right)^2 \right\}^{1/2} \quad (4.1)$$

where k are the model levels and σ_{var} is the standard deviation of that variable computed from all the profiles in the subset.

To find the N most dissimilar conditions within a subset, an iterative process is used:

1. A triplet of profiles (t, q, and $aermr06$) corresponding to one atmospheric condition is randomly selected from subset. This triplet is stored in a provisional calibration database. Only $aermr06$ is used here (and not $aermr04$ and $aermr05$) as it consists of the largest aerosol size range and has the biggest impact on TIR radiances.
2. A new triplet of profiles is randomly selected from the subset and the distances D_t, D_q, and $D_{aermr06}$ are computed between this new triplet and the other triplets in the provisional calibration database. The minimum values D_t^{min}, D_q^{min}, and $D_{aermr06}^{min}$ are computed.
3. The new triplet is stored in the provisional calibration database if D_t^{min}, D_q^{min}, and $D_{aermr06}^{min}$ meet the criteria for the minimum acceptable distance:

$$D_t^{min} + \mu_q D_q^{min} + \mu_{aermr06} D_{aermr06}^{min} > d \quad (4.2)$$

   The parameters μ_q and $\mu_{aermr06}$ are used to take into account the difference in vertical variability of temperature profiles and humidity and aerosol mixing ratio profiles. $\mu_q$takes a value of 1/9, following Chevallier et al. (2000) [83]. For $\mu_{aermr06}$ three different value were tested: 0.1, 0.2, and 0.3. An assessment of the three values is presented in Section 4.2.
4. Steps 2 and 3 are repeated until all profiles in the subset are tested.

At the end of these 4 steps a certain amount of triplets will have been stored in the provisional calibration database. If the amount of selected triplets is lower (higher) than the desired N then a lower (higher) value for d must be used. This process of adjusting d is iteratively repeated until the desired sample size is achieved (in this case 500, with a tolerance of ±10 profiles to simplify calculations). Since the values of D_t, D_q, and $D_{aermr06}$ depend on the distribution of $t(k)$, $q(k)$, and $aermr06(k)$ in the subset, the value of d will be different for each subset, which makes this a computationally intensive process.

The option of only applying the dissimilarity method to $aermr06$ profiles and then matching each obtained profile to t and q profiles of an already existing calibration database (such as that from Ermida & Trigo (2022) [84]) was considered. However, this could result in unrealistic conditions since dust aerosols are not typically present over the whole globe. Furthermore, matching between the pressure profiles of the aerosol data and the t and q data is a complex procedure and may introduce discrepancies in the optical depth of the aerosol profiles. Another option would be to apply the dissimilarity method to the $aermr06$ profiles and simply use the corresponding t and q profiles for the calibration database. This, however, can limit the representativeness of t and q profiles in the database, as will be shown in the next section.

4.2 DuAOD-dependent Calibration Database

The DuAOD-dependent calibration database constructed using the dissimilarity method will now be analyzed. First, the three possible values for $\mu_{aermr06}$ (0.1, 0.2, and 0.3) are assessed in their ability to select profiles that are representative of the variability within each subset. For this purpose, the dissimilarity method was run first for t and q profiles only (sample-tq), then for $aermr06$ profiles only (sample-$aermr06$), and lastly for the three variables combined (sample-$tqaermr06$) as described by Eq. (4.2). By doing so, sample-tq will have a selection of t and q profiles that is as representative as possible of a given subset, without being conditioned by the aerosol profiles. In the same way, sample-$aermr06$ will be maximally representative of the variability in $aermr06$ profiles, without being influenced by the temperature and humidity profiles. With these two samples as benchmarks, t and q profiles obtained in sample-$tqaermr06$ should be as close as possible to those from sample-tq, while $aermr06$ profiles as close as possible to those from sample-$aermr06$. Based on this qualitative metric, one of the three values of $\mu_{aermr06}$ will be chosen for the DuAOD-dependent GSW calibration.

Fig. 4.1 shows the selection of $aermr06$, q, and t profiles (first, second, and third row, respectively) in all samples (tq, $aermr06$, and $tqaermr06$ for the three values of $\mu_{aermr06}$, represented by different colors) from three distinct subsets (each column). The distribution of profiles in each sample is represented by the respective 25th, 50th, and 75th percentiles in each model level. Only model levels with relevant differences between the samples are shown, i.e. starting at level 48 for t and around 30 for q and $aermr06$. The three subsets displayed are all in the DuAOD class ranging from 0.2 to 0.4, while TCWV and Tskin vary between the bottom (0≤TCWV≤10 and 270≤Tskin≤290), medium (20≤TCWV≤30 and 290≤Tskin≤310), and upper (40≤TCWV≤50 and 310≤Tskin≤330) ranges. Other DuAOD classes are not shown as they have similar results — DuAOD from 0.2 to 0.4 represents an intermediate class. For ease of reading, 25th percentiles are plotted as dotted lines, the medians as solid lines, and the 75th percentiles as dashed lines, and the benchmark samples — sample-tq and sample-$aermr06$ — are plotted in grey and black, respectively, while the three different sample-$tqaermr06$ are plotted in distinctive colors.

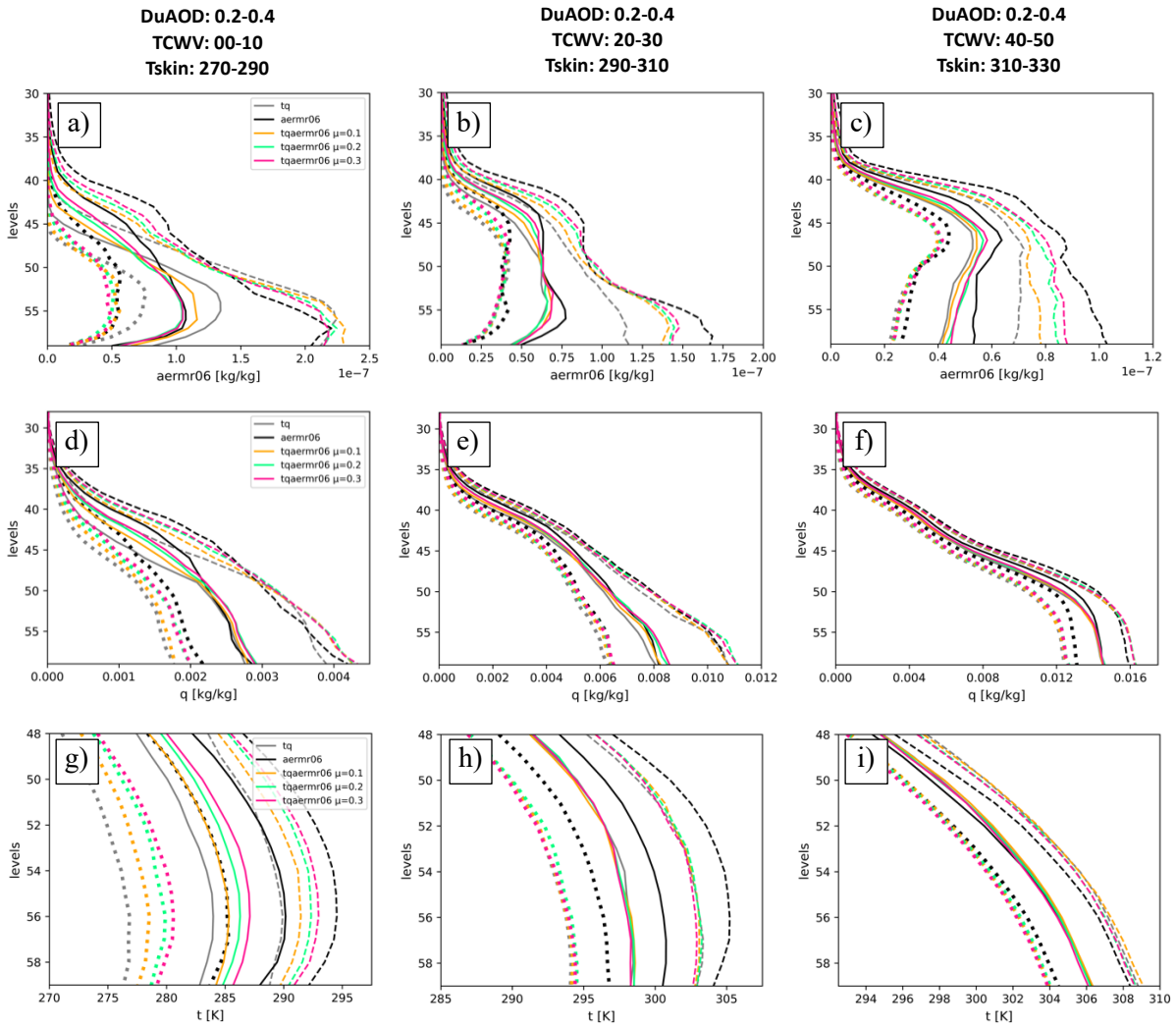

Figure 4.1 — Distribution of selected profiles of $aermr06$ (top panels), q (middle panels), and t (bottom panels) in sample-tq, sample-$aermr06$, and sample-$tqaermr06$ using three different values for $\mu_{aermr06}$, for three subsets (columns) of varying TCWV and Tskin. Represented are the 25th (dotted), 50th (solid), and 75th (dashed) percentiles of each sampling.

Firstly, analyzing the $aermr06$ profiles (Figs. 4.1(a)-(c)), it is interesting to note that the general shape of the profiles changes as TCWV and Tskin increase. Because the DuAOD class remains constant, the aerosol profiles are all inside the 0.2-0.4 DuAOD range when vertically integrated. Additionally, since the 25th, 50th, and 75th percentiles of this range are shown, 25th percentiles represent profiles with DuAOD≈0.25, 50th percentiles represent profiles DuAOD≈0.3, and 75th percentiles represent profiles with DuAOD≈0.35. Note that as TCWV and Tskin classes increase, the mixing ratio values (given by the x-axis) decrease slightly. This is compensated by mixing ratios increasing at higher altitudes. In fact, it can be noticed that for the low TCWV and Tskin class (Fig. 4.1(a)) the profiles have generally a maximum near the surface (around L57≈100 m), likely linked to a shallow boundary layer due to low surface temperatures; for the medium TCWV and Tskin class (Fig. 4.1(b)) the profiles develop a bimodality, maintaining the maximum close to the surface but also gaining a local maximum around L42≈4 km, which could be the result of a developing boundary layer; for the high TCWV and Tskin class (Fig. 4.1(c)) the profiles are well-mixed across the 4-km-high boundary layer characteristic of hot desert regions. Regarding the representation of $aermr06$ profiles by the different sampling schemes, it appears that all three variants of sample-$tqaermr06$ provide a good compromise between the

distributions of the two baselines samples (sample-tq and sample-$aermr06$) when these are similar, and are closer to sample-$aermr06$ when the baseline samples are more divergent. Naturally, using a larger value for $\mu_{aermr06}$ will cause the $aermr06$ profiles to have more weight when calculating the dissimilarity between conditions (Eq. (4.2)) and, therefore, the selected $aermr06$ profiles will be closer to the sample-$aermr06$ than if a smaller value for $\mu_{aermr06}$ were used.

Humidity profiles (Figs. 4.1(d)-(f)) also have an interesting progression as TCWV and Tskin classes increase. Evidently, as the TCWV class increases so do the maximum values of mixing ratio (x-axis). However, while in the low TCWV class the vertical distribution of q has a steady decrease with altitude, as the TCWV (and Tskin) class increases the q profiles tend to develop a mixed layer up to L50≈1 km. The increase in surface temperature definitely plays a role in this, as it governs the rate of convection and mixing. The fact that the mixed layer in Fig. 4.1(f) only reaches altitudes of 1 km, while the well-mixed layer of dust aerosols reaches altitudes of 4 km, may be linked to the different buoyancies of humid air and dust-aerosol-filled air. Looking closely at Fig. 4.1(c), it appears that dust aerosol clouds are kept at higher altitude, buoyant on a lower layer of moist atmosphere. In terms of the representativeness, the different samples are very similar to each other, the biggest discrepancies being at high altitudes (L47-L40) for the lowest TCWV and Tskin class Fig. 4.1(a). In this case the three variants of sample-$tqaermr06$ are a compromise between the two baseline samples.

The biggest differences between samples are in temperature profiles (Figs. 4.1(g)-(i)), especially for the low and medium TCWV and Tskin classes. An interesting characteristic of the t profile distributions is that their ranges are large for low TCWV and Tskin and tend to decrease for higher classes of TCWV an Tskin. This may be a consequence of the heat capacity of a very moist atmosphere being much higher than a drier atmosphere, or that locations where DuAOD values of 0.2-0.4 are common (i.e. in the regions surrounding the hot deserts) are subject to monsoon patterns where high humidity is generally coupled with high temperatures. Figs. 4.1(g) and (h) are a great example of how sample-$tqaermr06$ represents well the t profiles from the sample-tq and how lower values of $\mu_{aermr06}$ improves this representation as less weight is put on $aermr06$ profiles in the dissimilarity computations.

These three distinct subsets give a good indication that the addition of $aermr06$ profiles to the dissimilarity method provides acceptable results regarding the representation of the t, q, and $aermr06$ profiles in sample-$tqaermr06$, with some variation between subsets. Specifically, for $aermr06$ profiles when the TCWV and Tskin class is high or for t profiles when the TCWV and Tskin class is low the profile representation is not ideal and adjusting $\mu_{aermr06}$ can either improve the representation of $aermr06$ or t, not both simultaneously. Given that a compromise between representing well $aermr06$ or t must be made, the value chosen for $\mu_{aermr06}$ to construct the DuAOD-dependent calibration database is the intermediate one: $\mu_{aermr06} = 0.2$. Here it is important to note that since percentiles between sample-tq and sample-$aermr06$ can differ significantly, especially for t (e.g. Fig. 4.1(g)) and $aermr06$ profiles (e.g. Fig. 4.1(c)), it is not suitable to use the dissimilarity method on $aermr06$ profiles only and select the corresponding t and q profiles for the calibration database, as this would limit the robustness of the algorithm. The same applies for using the dissimilarity method on the t and q and selecting the corresponding $aermr06$ profiles. Therefore, the dissimilarity method must be used with all three variables, t, q, and $aermr06$, simultaneously.

Another way of assessing the representativeness of the calibration database and, therefore, the robustness of the algorithm produced, is by examining the distribution of simulated BTs for the selected conditions and comparing them with those from sample-tq and sample-$aermr06$, since BTs are the main input to the GSW algorithm. In particular, the BT mean values and the BT differences — the two main terms of Eq. (2.23) — are assessed. Fig. 4.2 shows histograms of BT mean values ($(BT_{10.8} + BT_{12.0})/2$) (top row) and histograms of BT differences ($BT_{10.8} - BT_{12.0}$) (bottom row) of the three sampling schemes (sample-$tqaermr06$ using $\mu_{aermr06}$=0.2) for the same three subsets as Fig. 4.1. As can be seen in both BT mean and BT difference histograms, the two baseline samples have slightly different distributions, which reflects the different range of conditions that each represents, and using sample-$tqaermr06$ ensures a compromise between the two.

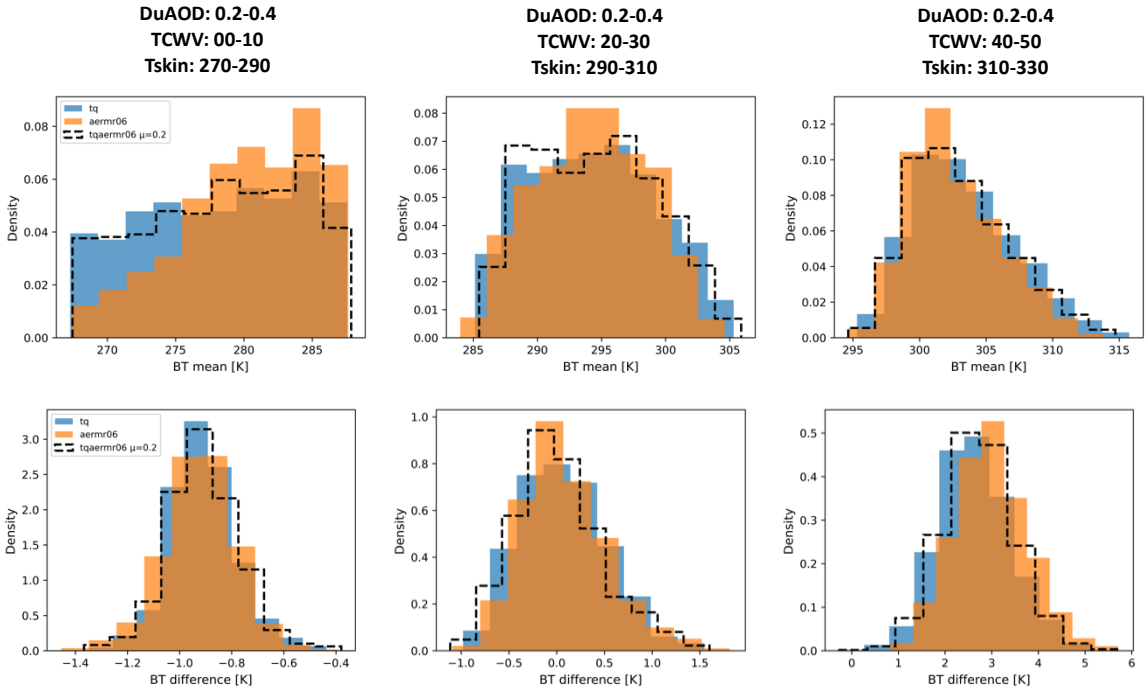

Figure 4.2 — Distribution of BT mean values (top row) and BT differences (bottom row) obtained using sample-tq, sample-$aermr06$, and sample-$tqaermr06$ with $\mu_{aermr06} = 0.2$ for three subsets (columns) of varying TCWV and Tskin.

Given the demonstrated capability of the dissimilarity method to simultaneously select t, q, and $aermr06$ profiles that are representative of the broad range of conditions present within a given class of TCWV, Tskin, and DuAOD, a DuAOD-dependent calibration database is created using $\mu_{aermr06} = 0.2$. Emissivities for the database where prescribed based on the landcover at the location of each profile, following Ermida & Trigo (2022) [84].

4.3 Calibration of DuAOD-dependent GSW Coefficients

The calibration database presented in the previous section is used to calibrate GSW coefficients that are not only dependent on TCWV and SZA, as is usually the case, but also on DuAOD. The simplest approach to include the effect of dust aerosols in the GSW is to keep the original formulation (Eq. 2.23) and calibrate the coefficients for different ranges of DuAOD. For the calibration process, 1/3 of the database is randomly selected and used to calibrate the coefficients, the remaining 2/3 is used for validation. Fig. 4.3 shows the GSW coefficients (Eq. (2.23)) obtained without considering dust aerosols, and respective root mean squared error (RMSE), that will be used as reference for the comparison with the DuAOD-dependent algorithm.

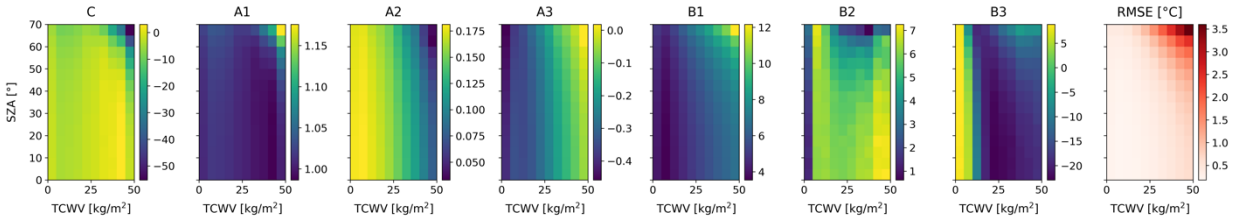

Figure 4.3 — Aerosol-free calibration of GSW coefficients and respective RMSE.

The DuAOD-dependent GSW coefficients are presented in Fig. 4.4. Compared to the aerosol-free coefficients (Fig. 4.3), the DuAOD-dependent coefficients' variation with TCWV and SZA is, in general, less smooth, showing stronger variations for higher DuAOD classes. In terms of the ranges of values, coefficients A_1, A_2, A_3, and B_1 are similar to originals, while C, B_2, and B_3 increase their ranges significantly. This indicates that the GSW adjusts to the radiative effect of dust aerosols by mostly modifying these three coefficients. This is not surprising, as B_2 and B_3 are associated to the differential absorption by the atmosphere (see Eq. (2.23)). Notably, the RMSE values increase for classes of higher DuAOD, which possibly indicates limitations in the GSW to simultaneously address the opposing effects of water vapor and dust aerosols.

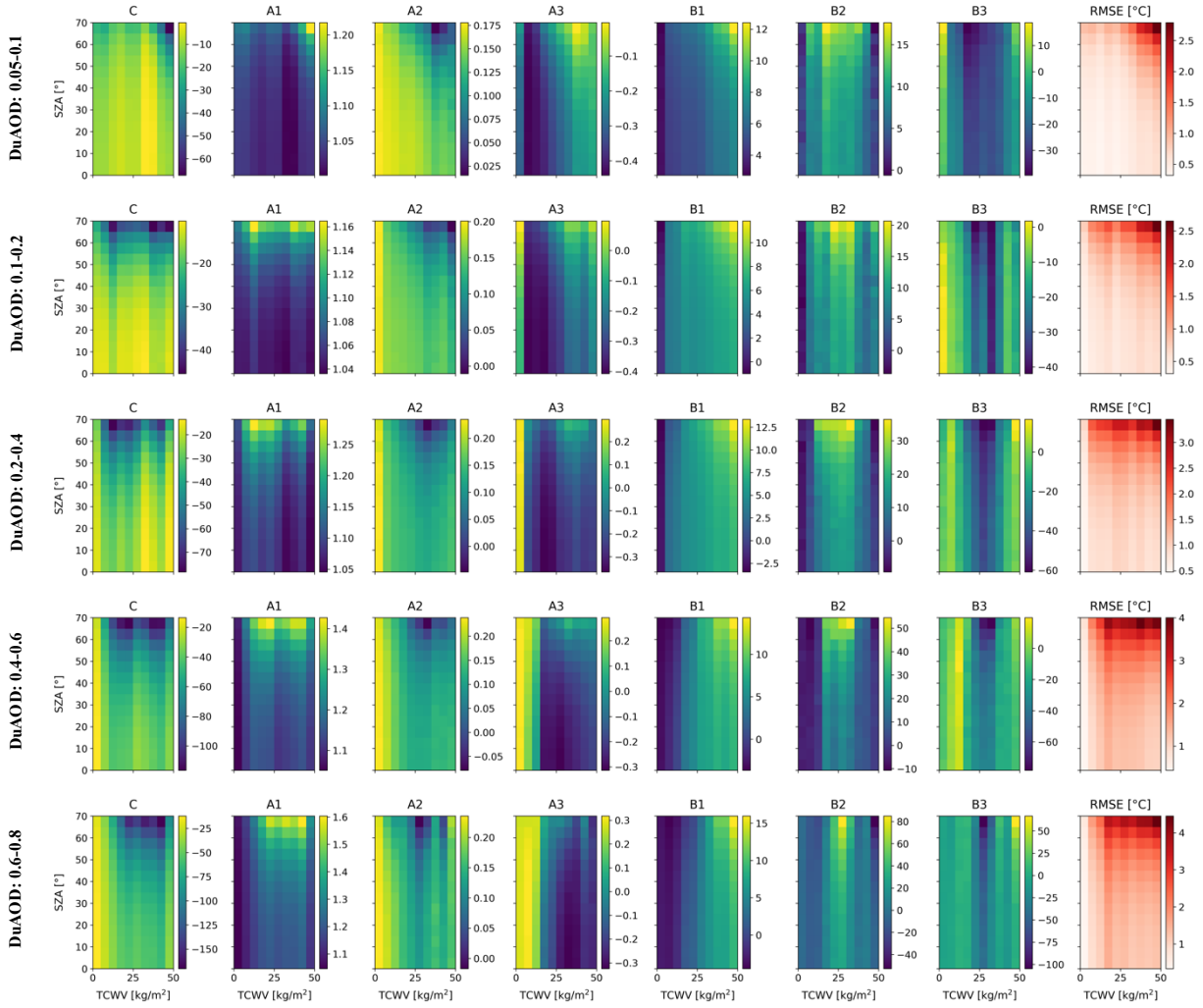

Figure 4.4 — DuAOD-dependent GSW coefficients and respective RMSE. Each row corresponds to a DuAOD class.

4.4 Improvements in LST estimation using a DuAOD-dependent GSW Algorithm

To evaluate the improved ability of the DuAOD-dependent GSW algorithm to estimate LST under increasingly higher values of DuAOD, the aerosol-free coefficients of the GSW (shown in Fig. 4.3) are used to derive LSTs from the validation data of the new DuAOD-dependent calibration database. The respective RMSEs are compared against the RMSEs of the DuAOD-dependent GSW for the different classes of DuAOD. Fig. 4.5 shows the differences in RMSE between the two GSW's (as aerosol-free minus DuAOD-dependent). Improvements between 1 °C and 2 °C for all TCWV and SZA can be seen for DuAOD as low as 0.2-0.4. For the next DuAOD class (0.4-0.6), improvements are above 2 °C for TCWV>30 kg/m^2 or SZA> 30°. For DuAOD above 0.6, the improvement is larger than 2 °C for any TCVW/SZA and larger than 3 °C starting at SZA=10°.

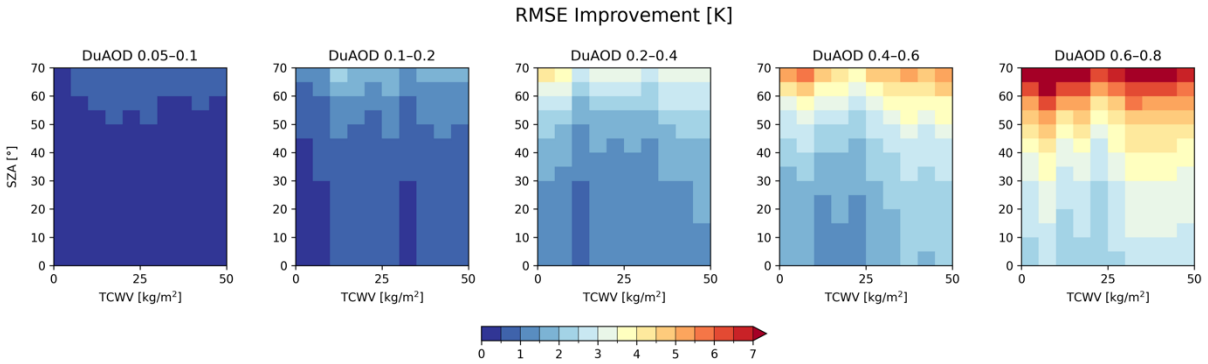

Figure 4.5 — RMSE difference between the aerosols-free and DuAOD-dependent GSW algorithms. Positive values indicate a reduction of the RMSE by the DuAOD-dependent algorithm.

The results presented above on the RMSE improvements are a good indication of the general scale of improvements that are achievable with a DuAOD-dependent GSW algorithm. As an indication of the potential area over which the use of such an algorithm could have significant benefits, Fig. 4.6 shows the locations with at least one occurrence of DuAOD≥0.4. The spatial extent of potential improvements is significant, primarily containing the major global deserts but also locations affected by advection of dust, such as southern Europe. This underscores the necessity of implementing an aerosol-robust LST retrievals algorithms and the benefits that could result from it.

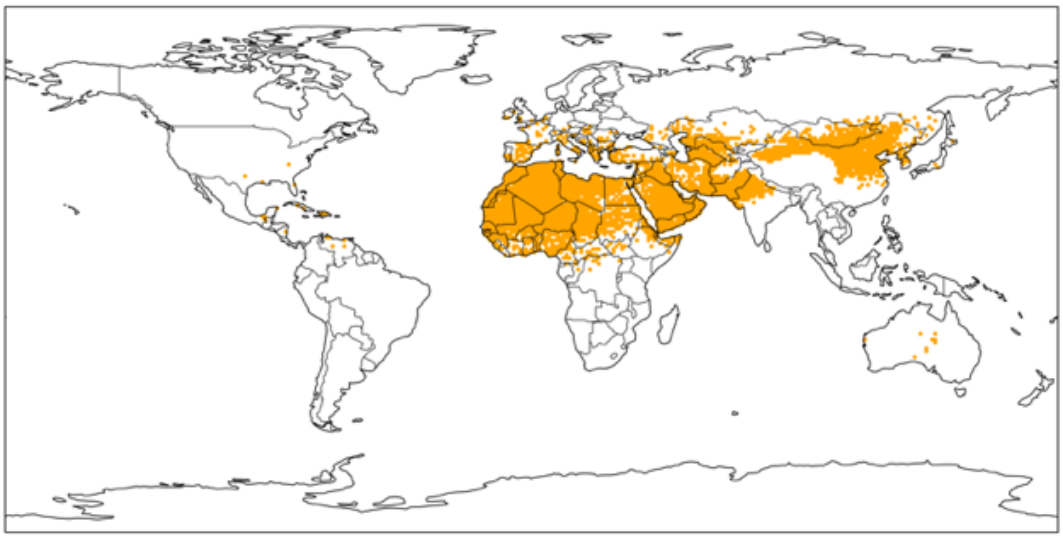

Figure 4.6 — Locations where CAMS DuAOD reaches values of 0.4 or above for the period of study (2019-2021).

Chapter 5 — Conclusions

In this dissertation the underestimation of remotely sensed TIR-based products in conditions of heavy dust aerosol loading evidenced by previous works is addressed. With that purpose, first an analysis of the effect of dust aerosols on TIR radiation is conducted to determine how the surface-emitted TIR radiation is affected as it propagates towards the TOA, and examine the contribution of atmospheric emission and multiple scattering to the radiation measured by the satellite sensor. This analysis relies on simulations using RTTOV (version 13), a fast RTM currently developed at NWP SAF.

When using RTTOV to simulate the effect of aerosols on the radiative transfer, two options are available for computing the multiple scattering by the aerosols: using the default solver with a Chou-scaling parametrization or the DOM solver. These two solving schemes were compared and DOM — the more accurate option for computing scattering but more computationally expensive — is found to have non-negligible biases when water vapor content and dust aerosol concentrations are low. Given these errors but wanting to exploit the superior capability of DOM to compute scattering by aerosols, Chou and DOM are used in conjunction when simulating TOA BTs in the presence of dust aerosols: aerosol-free Chou simulations are used to determine a baseline BT to which a BT shift caused by the dust aerosol is added, computed by the difference between DOM simulations with and without aerosols.

To analyze the radiative effect of dust aerosols in the TIR, RTTOV simulations are run using as input atmospheric profiles and surface variables for the Sahara Desert obtained from CAMS' EAC4 and ECMWF's ERA5 reanalyses, respectively. The simulated TOA BTs are examined first, in particular the BT differences between the two SEVIRI TIR channels (centered at 10.8 and 12.0 μm), which is a critical component of the GSW algorithm for LST estimation. BT differences (as $BT_{10.8}$– $BT_{12.0}$) are shown to decrease with increasing DuAOD in contrast to the usual increase with TCWV, a behavior that is exploited by the GSW algorithm to account for the atmospheric attenuation caused by water vapor. The behavior of BT differences with DuAOD, which is consistent with the optical properties of dust aerosols, is the main driver of underestimations of LST by the GSW algorithm when dust aerosol concentration are high: since the GSW relies on BT differences to determine the deficit in radiance reaching the TOA and thus estimate the surface-emitted TIR radiation (and therefore LST), if BT differences are lower than usual for a given TCWV due to the presence of dust aerosols, then the GSW will underestimate the amount of atmospheric attenuation experienced by the surface-emitted TIR radiation, thus underestimating the surface radiance and, consequently, LST.

This behavior of BT differences with DuAOD is driven by the changes in SEVIRI channel transmittances with increasing dust aerosol concentration. With increasing DuAOD the transmissivity of channel 10.8 μm decreases in a more pronounced way than that of channel 12.0 μm, which is consistent with the imaginary part of the complex index of refraction of dust aerosols being higher at 10.8 than at 12.0 μm. Although the transmissivity decreases by about 40% in channel 10.8 μm for a DuAOD around 2.0, the difference in TOA radiances only decreases by about 4%. This small difference in TOA radiances despite the intense decrease in surface radiance reaching TOA due to the lower transmissivities is explained by a sharp increase in atmospheric emission caused by the aerosols.

The differential absorption of TIR radiation by dust aerosols shown in this analysis (i.e., a more pronounced absorption at 10.8 μm than the 12.0 μm) is a feature that can be used for addressing the effect dust aerosols on LST retrievals. In fact, the GSW algorithm exploits differential absorption by water vapor to account for its attenuation of the surface-emitted radiation and correctly estimate LST.

Therefore, although the differential absorption by water vapor is in the opposite direction of that by dust aerosols, a GSW calibrated with dust aerosol information is likely to improve LST estimations under moderate-to-high dust aerosol concentrations.

In order to assess the ability of a GSW algorithm calibrated with dust aerosol information to estimate LST under such conditions, a novel GSW calibration is explored using DuAOD-dependent GSW coefficients. This requires a calibration database representing a broad range of atmospheric and surface conditions for various classes of DuAOD to guarantee the robustness of the algorithm in all possible scenarios. Selection of these conditions is performed using a methodology which calculates the dissimilarity between two atmospheric conditions based on the profiles of temperature, humidity, and dust aerosols. With this database a DuAOD-dependent GSW algorithm is calibrated and compared against an aerosol-free GSW. The results are encouraging, indicating improvements in LST accuracy by at least 2 °C for DuAOD $\geq$ 0.4 which are optical depths that occur frequently over many areas around the globe (Fig. 4.6).

Despite these promising results, some further developments may be considered in future work. For instance, the accuracy of LST retrievals using a DuAOD-dependent GSW algorithm under heavy dust aerosol loadings will depend on the accuracy of DuAOD forecasts used. A sensitivity analysis must be performed to understand the impact of DuAOD uncertainties on the LST accuracies. This analysis will also help determine the threshold of dust aerosol concentrations above which the aerosol-robust GSW algorithm has a better performance than a regular GSW, by considering the uncertainties of the algorithms and the DuAOD forecasts. Moreover, since the atmospheric correction performed by the GSW assumes a linearity of the differential absorption by water vapor in the TIR, it is important to investigate whether this linearity also exists for dust aerosols. If this is not the case then a different formulation of the split-window may have a better performance than using the GSW for retrievals when concentrations of dust aerosols are high.

Bibliography

[1] Z. Su, "The Surface Energy Balance System (SEBS) for estimation of turbulent heat fluxes," *Hydrol. Earth Syst. Sci.*, vol. 6, no. 1, 2002, doi: 10.5194/hess-6-85-2002.

[2] X. Zhan and W. P. Kustas, "A coupled model of land surface CO2 and energy fluxes using remote sensing data," *Agric. For. Meteorol.*, vol. 107, no. 2, 2001, doi: 10.1016/S0168-1923(00)00229-X.

[3] R. D. Crago and R. J. Qualls, "Use of land surface temperature to estimate surface energy fluxes: Contributions of Wilfried Brutsaert and collaborators," *Water Resour. Res.*, vol. 50, no. 4, 2014, doi: 10.1002/2013WR015223.

[4] J. Sun, G. D. Salvucci, and D. Entekhabi, "Estimates of evapotranspiration from MODIS and AMSR-E land surface temperature and moisture over the Southern Great Plains," *Remote Sens. Environ.*, vol. 127, 2012, doi: 10.1016/j.rse.2012.08.020.

[5] J. D. Kalma, T. R. McVicar, and M. F. McCabe, "Estimating land surface evaporation: A review of methods using remotely sensed surface temperature data," *Surveys in Geophysics*, vol. 29, no. 4–5. 2008, doi: 10.1007/s10712-008-9037-z.

[6] L. Olivera-Guerra, C. Mattar, O. Merlin, C. Durán-Alarcón, A. Santamaría-Artigas, and R. Fuster, "An operational method for the disaggregation of land surface temperature to estimate actual evapotranspiration in the arid region of Chile," *ISPRS J. Photogramm. Remote Sens.*, vol. 128, 2017, doi: 10.1016/j.isprsjprs.2017.03.014.

[7] A. J. Arnfield, "Two decades of urban climate research: A review of turbulence, exchanges of energy and water, and the urban heat island," *Int. J. Climatol.*, vol. 23, no. 1, 2003, doi: 10.1002/joc.859.

[8] J. A. Voogt and T. R. Oke, "Thermal remote sensing of urban climates," *Remote Sens. Environ.*, vol. 86, no. 3, 2003, doi: 10.1016/S0034-4257(03)00079-8.

[9] M. Bokaie, M. K. Zarkesh, P. D. Arasteh, and A. Hosseini, "Assessment of Urban Heat Island based on the relationship between land surface temperature and Land Use/ Land Cover in Tehran," *Sustain. Cities Soc.*, vol. 23, 2016, doi: 10.1016/j.scs.2016.03.009.

[10] A. Karnieli *et al.*, "Use of NDVI and land surface temperature for drought assessment: Merits and limitations," *J. Clim.*, vol. 23, no. 3, 2010, doi: 10.1175/2009JCLI2900.1.

[11] F. N. Kogan, "Operational space technology for global vegetation assessment," *Bull. Am. Meteorol. Soc.*, vol. 82, no. 9, 2001, doi: 10.1175/1520-0477(2001)082<1949:OSTFGV>2.3.CO;2.

[12] D. A. Sims *et al.*, "A new model of gross primary productivity for North American ecosystems based solely on the enhanced vegetation index and land surface temperature from MODIS," *Remote Sens. Environ.*, vol. 112, no. 4, 2008, doi: 10.1016/j.rse.2007.08.004.

[13] N. T. Sona, C. F. Chen, C. R. Chen, L. Y. Chang, and V. Q. Minh, "Monitoring agricultural drought in the lower mekong basin using MODIS NDVI and land surface temperature data," *Int. J. Appl. Earth Obs. Geoinf.*, vol. 18, no. 1, 2012, doi: 10.1016/j.jag.2012.03.014.

[14] S. Sruthi and M. A. M. Aslam, "Agricultural Drought Analysis Using the NDVI and Land Surface Temperature Data; a Case Study of Raichur District," *Aquat. Procedia*, vol. 4, 2015, doi: 10.1016/j.aqpro.2015.02.164.

[15] C. Quintano, A. Fernández-Manso, L. Calvo, E. Marcos, and L. Valbuena, "Land surface temperature as potential indicator of burn severity in forest Mediterranean ecosystems," *Int. J. Appl. Earth Obs. Geoinf.*, vol. 36, 2015, doi: 10.1016/j.jag.2014.10.015.

[16] L. Vlassova, F. Pérez-Cabello, M. R. Mimbrero, R. M. Llovería, and A. García-Martín, "Analysis of the relationship between land surface temperature and wildfire severity in a series of landsat images," *Remote Sens.*, vol. 6, no. 7, 2014, doi: 10.3390/rs6076136.

[17] Z. L. Li *et al.*, "Satellite-derived land surface temperature: Current status and perspectives," *Remote Sensing of Environment*, vol. 131. 2013, doi: 10.1016/j.rse.2012.12.008.

[18] I. F. Trigo, S. L. Ermida, J. P. A. Martins, C. M. Gouveia, F. M. Göttsche, and S. C. Freitas, "Validation and consistency assessment of land surface temperature from geostationary and polar orbit platforms: SEVIRI/MSG and AVHRR/Metop," *ISPRS J. Photogramm. Remote Sens.*, vol. 175, 2021, doi: 10.1016/j.isprsjprs.2021.03.013.

[19] P. C. Guillevic *et al.*, "Validation of Land Surface Temperature products derived from the Visible Infrared Imaging Radiometer Suite (VIIRS) using ground-based and heritage satellite measurements," *Remote Sens. Environ.*, vol. 154, 2014, doi: 10.1016/j.rse.2014.08.013.

[20] N. K. Malakar and G. C. Hulley, "A water vapor scaling model for improved land surface temperature and emissivity separation of MODIS thermal infrared data," *Remote Sens. Environ.*, vol. 182, 2016, doi: 10.1016/j.rse.2016.04.023.

[21] M. A. Martin, D. Ghent, A. C. Pires, F. M. Göttsche, J. Cermak, and J. J. Remedios, "Comprehensive in situ validation of five satellite land surface temperature data sets over multiple stations and years,"

Remote Sens., vol. 11, no. 5, 2019, doi: 10.3390/rs11050479.
[22] S. B. Duan *et al.*, "Validation of Collection 6 MODIS land surface temperature product using in situ measurements," *Remote Sens. Environ.*, vol. 225, 2019, doi: 10.1016/j.rse.2019.02.020.
[23] Z. Wan, *MODIS land-surface temperature algorithm theoretical basis document (LST ATBD). Institute for Computational Earth System Science, Santa Barbara.*, no. April. 1999.
[24] F. Stante, S. L. Ermida, C. C. DaCamara, F.-M. Göttsche, and I. F. Trigo, "Impact of High Concentrations of Saharan Dust Aerosols on Infrared-Based Land Surface Temperature Products," *IEEE J. Sel. Top. Appl. Earth Obs. Remote Sens.*, vol. 16, pp. 4064–4079, 2023, doi: 10.1109/JSTARS.2023.3263374.
[25] M. Griggs, "A method to correct satellite measurements to sea surface temperature for the effects of atmospheric aerosols.," *J. Geophys. Res.*, vol. 90, no. D7, 1985, doi: 10.1029/JD090iD07p12951.
[26] C. Walton, "Satellite measurement of sea surface temperature in the presence of volcanic aerosols (Hawaii, Gulf-of-Mexico).," *J. Clim. Appl. Meteorol.*, vol. 24, no. 6, 1985.
[27] L. Xu and W. L. Smith, "Numerical simulation of the influence of volcanic aerosols on VAS derived SST determinations," *Appl. Opt.*, vol. 25, no. 7, 1986, doi: 10.1364/ao.25.001137.
[28] S. J. Brown, A. R. Harris, I. M. Mason, and A. M. Závody, "New aerosol robust sea surface temperature algorithms for the along-track scanning radiometer," *J. Geophys. Res. Ocean.*, vol. 102, no. C13, 1997, doi: 10.1029/97JC01192.
[29] B. Luo, P. J. Minnett, C. Gentemann, and G. Szczodrak, "Improving satellite retrieved night-time infrared sea surface temperatures in aerosol contaminated regions," *Remote Sens. Environ.*, vol. 223, 2019, doi: 10.1016/j.rse.2019.01.009.
[30] D. A. May, L. L. Stowe, J. D. Hawkins, and E. P. McClain, "A correction for Saharan dust effects on satellite sea surface temperature measurements," *J. Geophys. Res.*, vol. 97, no. C3, 1992, doi: 10.1029/91JC02987.
[31] C. J. Merchant, A. R. Harris, M. J. Murray, and A. M. Závody, "Toward the elimination of bias in satellite retrievals of sea surface temperature 1. Theory, modeling and interalgorithm comparison," *Journal of Geophysical Research: Oceans*, vol. 104, no. C10. 1999, doi: 10.1029/1999jc900105.
[32] C. J. Merchant, O. Embury, P. Le Borgne, and B. Bellec, "Saharan dust in nighttime thermal imagery: Detection and reduction of related biases in retrieved sea surface temperature," *Remote Sens. Environ.*, vol. 104, no. 1, 2006, doi: 10.1016/j.rse.2006.03.007.
[33] C. J. Merchant and O. Embury, "Adjusting for desert-dust-related biases in a climate data record of sea surface temperature," *Remote Sensing*, vol. 12, no. 16. 2020, doi: 10.3390/RS12162554.
[34] N. R. Nalli and L. L. Stowe, "Aerosol correction for remotely sensed sea surface temperatures from the National Oceanic and Atmospheric Administration advanced very high resolution radiometer," *J. Geophys. Res. Ocean.*, vol. 107, no. 10, 2002, doi: 10.1029/2001jc001162.
[35] X. Quan, H. L. Huang, L. Zhang, E. Weisz, and X. Cao, "Sensitive detection of aerosol effect on simulated IASI spectral radiance," *J. Quant. Spectrosc. Radiat. Transf.*, vol. 122, 2013, doi: 10.1016/j.jqsrt.2012.05.002.
[36] X. Fan *et al.*, "Extension of the generalized split-window algorithm for land surface temperature retrieval to atmospheres with heavy dust aerosol loading," *IEEE J. Sel. Top. Appl. Earth Obs. Remote Sens.*, vol. 8, no. 2, 2015, doi: 10.1109/JSTARS.2014.2358584.
[37] C. Gao *et al.*, "Study of aerosol influence on nighttime land surface temperature retrieval based on two methods," *Adv. Meteorol.*, vol. 2015, 2015, doi: 10.1155/2015/496458.
[38] X. Fan, G. Nie, H. Wu, and B.-H. Tang, "Estimation of land surface temperature from three thermal infrared channels of MODIS data for dust aerosol skies," *Opt. Express*, vol. 26, no. 4, 2018, doi: 10.1364/oe.26.004148.
[39] E. Zhao, C. Gao, and Y. Yao, "New land surface temperature retrieval algorithm for heavy aerosol loading during nighttime from Gaofen-5 satellite data," *Opt. Express*, vol. 28, no. 2, 2020, doi: 10.1364/oe.382813.
[40] A. LABBI, "A study of the impact of aerosols on the estimation of land surface temperature from space using simulation of satellite data," *Turkish J. Remote Sens. GIS*, 2021, doi: 10.48123/rsgis.839293.
[41] L. Bi, S. Ding, R. Zong, and B. Yi, "Examining Asian dust refractive indices for brightness temperature simulations in the 650–1135 cm−1 spectral range," *J. Quant. Spectrosc. Radiat. Transf.*, vol. 247, 2020, doi: 10.1016/j.jqsrt.2020.106945.
[42] I. Tegen, P. Hollrig, M. Chin, I. Fung, D. Jacob, and J. Penner, "Contribution of different aerosol species to the global aerosol extinction optical thickness: Estimates from model results," *J. Geophys. Res. Atmos.*, vol. 102, no. 20, 1997, doi: 10.1029/97jd01864.
[43] M. Gavrouzou, N. Hatzianastassiou, A. Gkikas, M. B. Korras-Carraca, and N. Mihalopoulos, "A global climatology of dust aerosols based on satellite data: Spatial, seasonal and inter-annual patterns over the period 2005–2019," *Remote Sens.*, vol. 13, no. 3, 2021, doi: 10.3390/rs13030359.

[44] K. K. Voss and A. T. Evan, “A new satellite-based global climatology of dust aerosol optical depth,” *J. Appl. Meteorol. Climatol.*, vol. 59, no. 1, 2020, doi: 10.1175/JAMC-D-19-0194.1.
[45] I. F. Trigo *et al.*, “The Satellite Application Facility for Land Surface Analysis,” *Int. J. Remote Sens.*, vol. 32, no. 10, pp. 2725–2744, May 2011, doi: 10.1080/01431161003743199.
[46] I. F. Trigo, I. T. Monteiro, F. Olesen, and E. Kabsch, “An assessment of remotely sensed land surface temperature,” *J. Geophys. Res. Atmos.*, vol. 113, no. 17, 2008, doi: 10.1029/2008JD010035.
[47] Z. Wan and J. Dozier, “A generalized split-window algorithm for retrieving land-surface temperature from space,” *IEEE Trans. Geosci. Remote Sens.*, vol. 34, no. 4, 1996, doi: 10.1109/36.508406.
[48] Z. Wan, S. Hook, and G. Hulley, “MODIS/Aqua Land Surface Temperature/Emissivity Daily L3 Global 0.05Deg CMG V061 [Data set]. NASA EOSDIS Land Processes DAAC.” 2021, doi: 10.5067/MODIS/MYD11C1.061.
[49] Z. Wan, S. Hook, and G. Hulley, “MODIS/Terra Land Surface Temperature/Emissivity Daily L3 Global 0.05Deg CMG V061 [Data set]. NASA EOSDIS Land Processes DAAC.” 2021, doi: 10.5067/MODIS/MOD11C1.061.
[50] G. Hulley and S. Hook, “MODIS/Aqua Land Surface Temperature/3-Band Emissivity Daily L3 Global 0.05Deg CMG V061 [Data set]. NASA EOSDIS Land Processes DAAC.” 2021, doi: 10.5067/MODIS/MYD21C1.061.
[51] G. Hulley and S. Hook, “MODIS/Terra Land Surface Temperature/3-Band Emissivity Daily L3 Global 0.05Deg CMG V061 [Data set]. NASA EOSDIS Land Processes DAAC.” 2021, doi: 10.5067/MODIS/MOD21C1.061.
[52] D. Anding and R. Kauth, “Estimation of sea surface temperature from space,” *Remote Sens. Environ.*, vol. 1, no. 4, pp. 217–220, 1970, doi: 10.1016/S0034-4257(70)80002-5.
[53] D. Q. Wark, G. Yamamoto, and J. H. Lienesch, “Methods of Estimating Infrared Flux and Surface Temperature from Meteorological Satellites,” *J. Atmos. Sci.*, vol. 19, no. 5, 1962, doi: 10.1175/1520-0469(1962)019<0369:moeifa>2.0.co;2.
[54] A. H. Glaser, E. S. Merritt, R. Wexler, and J. Widger, W. K., “The Applicability of TIROS and Nimbus Data to Investigation of the Feasibility of Sea Surface Remperature Measurements from Satellites,” 1965.
[55] J. R. Greaves, R. Wexler, and C. J. . Bowley, “The Feasibility of Sea Surface Temperature Determination using Satellite Infrared Data - NASA Report,” 1966.
[56] L. J. Allison and J. S. Kennedy, “An Evaluation of Sea Surface Temperature as Measured by the Nimbus I High Resolution Infrared Radiometer - NASA Technical Note,” 1967.
[57] G. Warnecke, L. J. Allison, and L. L. Foshee, “Observations of Sea Surface Temperatures and Ocean Currents from Nimbus II - NASA Report,” 1967.
[58] W. L. Smith, P. K. Rao, R. Koffler, and W. R. Curtis, “The Determination of Sea-Surface Temperature form Satellite High Resolution Infrared Window Radiation Measurements,” *Mon. Weather Rev.*, vol. 98, no. 8, 1970, doi: 10.1175/1520-0493(1970)098<0604:tdosst>2.3.co;2.
[59] K. N. Liou, *An Introduction to Atmospheric Radiation (Second Edition)*, vol. 84. 2002.
[60] C. Prabhakara, B. J. Conrath, and V. G. Kunde, “Estimation of Sea Surface Temperature from Remote Measurements in the 11-13um Window Region — Goddard Space Flight Center Report,” 1972.
[61] F. Becker and Z. L. Li, “Towards a local split window method over land surfaces,” *Int. J. Remote Sens.*, vol. 11, no. 3, 1990, doi: 10.1080/01431169008955028.
[62] F. Becker, “The impact of spectral emissivity on the measurement of land surface temperature from a satellite,” *Int. J. Remote Sens.*, vol. 8, no. 10, 1987, doi: 10.1080/01431168708954793.
[63] Z. Wan and J. Dozier, “Land-Surface Temperature Measurement from Space: Physical Principles and Inverse Modeling,” *IEEE Transactions on Geoscience and Remote Sensing*, vol. 27, no. 3. 1989, doi: 10.1109/36.17668.
[64] D. S. Kimes, “Azimuthal radiometric temperature measurements of wheat canopies,” *Appl. Opt.*, vol. 20, no. 7, 1981, doi: 10.1364/ao.20.001119.
[65] I. Trigo *et al.*, “Algorithm Theoretical Basis Document for Land Surface Temperature (LST) — LSA SAF Report,” 2018.
[66] E. Borbas, S. W. Seemann, H.-L. Huang, J. Li, and W. P. Menzel, “Global profile training database for satellite regression retrievals with estimates of skin temperature and emissivity,” *Int. ATOVS Study Conf.*, 2005.
[67] F. E. Volz, “Infrared Optical Constants of Ammonium Sulfate, Sahara Dust, Volcanic Pumice, and Flyash,” *Appl. Opt.*, vol. 12, no. 3, 1973, doi: 10.1364/ao.12.000564.
[68] F. E. Volz, “Infrared Refractive Index of Atmospheric Aerosol Substances,” *Appl. Opt.*, vol. 11, no. 4, 1972, doi: 10.1364/ao.11.000755.
[69] N. Mahowald *et al.*, “The size distribution of desert dust aerosols and its impact on the Earth system,” *Aeolian Research*, vol. 15. 2014, doi: 10.1016/j.aeolia.2013.09.002.

[70] R. Saunders *et al.*, “An update on the RTTOV fast radiative transfer model (currently at version 12),” *Geosci. Model Dev.*, vol. 11, no. 7, 2018, doi: 10.5194/gmd-11-2717-2018.
[71] M. Matricardi, “The inclusion of aerosols and clouds in RTIASI, the ECMWF fast radiative transfer model for the infrared atmospheric sounding interferometer — ECMWF Report,” 2005.
[72] J. Hocking, “A visible/infrared multiple-scattering model for RTTOV — NWP SAF Report,” 2016.
[73] R. Saunders *et al.*, “RTTOV-12 Science and Validation Report — NWP SAF,” 2017.
[74] R. Saunders *et al.*, “RTTOV-13 Science and Validation Report — NW SAF,” 2020.
[75] M. D. Chou, K. T. Lee, S. C. Tsay, and Q. Fu, “Parameterization for cloud longwave scattering for use in atmospheric models,” *J. Clim.*, vol. 12, no. 1, 1999, doi: 10.1175/1520-0442-12.1.159.
[76] W. Zdunkowski, T. Trautmann, and A. Bott, *Radiation in the atmosphere: A course in theoretical meteorology*, vol. 9780521871075. 2007.
[77] K. Stamnes, S.-C. Tsay, W. Wiscombe, and K. Jayaweera, “Numerically stable algorithm for discrete-ordinate-method radiative transfer in multiple scattering and emitting layered media,” *Appl. Opt.*, vol. 27, no. 12, 1988, doi: 10.1364/ao.27.002502.
[78] K.-N. Liou, “A Numerical Experiment on Chandrasekhar’s Discrete-Ordinate Method for Radiative Transfer: Applications to Cloudy and Hazy Atmospheres,” *J. Atmos. Sci.*, vol. 30, no. 7, 1973, doi: 10.1175/1520-0469(1973)030<1303:aneocd>2.0.co;2.
[79] H. Hersbach *et al.*, “The ERA5 global reanalysis,” *Q. J. R. Meteorol. Soc.*, vol. 146, no. 730, 2020, doi: 10.1002/qj.3803.
[80] A. Inness *et al.*, “The CAMS reanalysis of atmospheric composition,” *Atmos. Chem. Phys.*, vol. 19, no. 6, 2019, doi: 10.5194/acp-19-3515-2019.
[81] L. F. Peres and C. C. DaCamara, “Emissivity maps to retrieve land-surface temperature from MSG/SEVIRI,” *IEEE Trans. Geosci. Remote Sens.*, vol. 43, no. 8, 2005, doi: 10.1109/TGRS.2005.851172.
[82] J. Hocking, R. Saunders, A. Geer, and J. Vidot, “RTTOV v13 Users Guide — NWP SAF Report,” 2021.
[83] F. Chevallier, A. Chédin, F. Cheruy, and J. J. Morcrette, “TIGR-like atmospheric-profile databases for accurate radiative-flux computation,” *Q. J. R. Meteorol. Soc.*, vol. 126, no. 563, 2000, doi: 10.1002/qj.49712656319.
[84] S. L. Ermida and I. F. Trigo, “A Comprehensive Clear-Sky Database for the Development of Land Surface Temperature Algorithms,” *Remote Sensing*, vol. 14, no. 10. 2022, doi: 10.3390/rs14102329.